International Journal of Hyperthermia

ISSN: 0265-6736 (Print) 1464-5157 (Online) Journal homepage: www.tandfonline.com/journals/ihyt20

New analytical and hybrid heat transfer models for thermal ablation procedures validated by MRI thermometry

Mariana De Melo Antunes, Ida Burgers, Valéry Ozenne, Luigi Nardone, Max Seidensticker, Olaf Dietrich, Manon Desclides, Bruno Quesson, Andrzej Kusiak, Sandro Metrevelle Marcondes de Lima e Silva & Jean-Luc Battaglia

To cite this article: Mariana De Melo Antunes, Ida Burgers, Valéry Ozenne, Luigi Nardone, Max Seidensticker, Olaf Dietrich, Manon Desclides, Bruno Quesson, Andrzej Kusiak, Sandro Metrevelle Marcondes de Lima e Silva & Jean-Luc Battaglia (2025) New analytical and hybrid heat transfer models for thermal ablation procedures validated by MRI thermometry, International Journal of Hyperthermia, 42:1, 2594943, DOI: 10.1080/02656736.2025.2594943

To link to this article: https://doi.org/10.1080/02656736.2025.2594943

INTERNATIONAL JOURNAL OF HYPERTHERMIA
2025, VOL. 42, NO. 1, 2594943
https://doi.org/10.1080/02656736.2025.2594943

New analytical and hybrid heat transfer models for thermal ablation procedures validated by MRI thermometry

Mariana De Melo Antunes[a,b], Ida Burgers[b], Valéry Ozenne[c], Luigi Nardone[d,e], Max Seidensticker[d], Olaf Dietrich[d], Manon Desclides[c], Bruno Quesson[c], Andrzej Kusiak[b], Sandro Metrevelle Marcondes de Lima e Silva[a] and Jean-Luc Battaglia[b]

[a]Heat Transfer Laboratory – LabTC, Institute of Mechanical Engineering, Campus Professor José Rodrigues Seabra, Federal University of Itajubá, Itajubá, Brazil; [b]Univ. Bordeaux, CNRS, Bordeaux INP, I2M, UMR 5295, F-33400, Talence, France; [c]Univ. Bordeaux, CNRS, CRMSB, UMR 5536, F-33000, Bordeaux, France; [d]Department of Radiology, LMU University Hospital, LMU Munich, Munich, Germany; [e]Department of Medicine, Institute of Radiology, University of Udine, Udine, Italy

ABSTRACT

Objective: This study proposes analytical and hybrid models for fast and accurate temperature field reconstruction in microwave ablation (MWA), laser interstitial thermal therapy (LITT), and radiofrequency ablation (RFA), aiming at future real-time clinical use.

Materials and methods: The proposed approach combines spatial variable transformation and the Laplace transform for time-dependent terms, with finite difference techniques. A 1 mm isotropic grid represents the voxel network. To ensure accurate temperature representation, voxel-averaged temperatures are computed by integrating the solution of the bioheat equation, under spherical symmetry, over voxel bounds. To approximate the elongated ablation zone, the central circumference of the spherical model is repeated and incorporated into a hemisphere-based geometry. Simulated temperature fields are aligned with experimental MRI data using Advanced Normalization Tools (ANTs). All experiments were conducted *ex vivo*: MWA in bovine liver, and LITT and RFA in agar phantoms. Regions of interest (ROIs) include voxels with significant thermal variation. Heat source parameters are estimated by minimizing the quadratic difference between simulated and MRI-derived temperatures via a spatiotemporal objective function

Results: Across all modalities, over 83–98% of voxels presented RMSE $\leq$ 1°C, with few exceeding 10°C. LITT showed the best overall agreement. Total simulation and alignment per repetitions required under 0.3 s, significantly below MRI repetition time, enabling potential intraoperative use.

Conclusion: Although approximate and not yet ready for *in vivo* clinical application, the proposed models offer fast, voxel-level temperature reconstructions. Their computational efficiency supports further development toward real-time monitoring and procedural adjustment during thermal ablation.

ARTICLE HISTORY
Received 29 April 2025
Revised 6 October 2025
Accepted 11 November 2025

KEYWORDS
Thermal ablation; microwave ablation; radio-frequency ablation; laser ablation; thermal modeling; analytical-based methods

1. Introduction

Recognized as a rapidly emerging and promising alternative treatment, thermal ablation is now used as a first-line treatment in both curative and palliative [1] care for benign and malignant tumors [2–4]. The procedure involves the destruction of targeted tissue using extreme temperatures, either considerably higher (hyperthermia) or considerably lower (hypothermia) than body temperature. For both, the ideal energy deposition is focused on the area in and around the tumor while preserving the healthy tissue in the surroundings.

CONTACT Mariana De Melo Antunes marianamelo@unifei.edu.br Heat Transfer Laboratory – LabTC, Institute of Mechanical Engineering, Campus Professor José Rodrigues Seabra, Federal University of Itajubá, BPS Avenue 1303, Itajubá, MG, Brazil

Supplemental data for this article can be accessed online at https://doi.org/10.1080/02656736.2025.2594943.

In this context, Magnetic Resonance Imaging (MRI) thermometry has emerged as a powerful tool to non-invasively monitor temperature changes (up to 100 °C) during thermal ablation procedures with a temporal resolution of the order of a second. MR thermal imaging has established itself in interventional MRI as the best tool to account for the formation and extension of the lesion during thermal ablation procedures [5–10]. However, real-time quantitative MRI-based temperature mapping techniques are hampered by many limitations and its potential is still largely under-exploited, particularly when it comes to making this treatment completely customizable. First, the relative uncertainty of temperature measurements by MRI is significant. Secondly, the used devices (systematically with RFA and MWA probes, more moderately for LITT) generates susceptibility artifacts from the metallic probes [11] on the images. This has direct consequences on the quantification of the temperature for voxels located in the immediate vicinity of the device (lack of information) where the heating is the strongest. Third, MRI thermometry only provides information on the evolution of the average temperature per voxel. This masks the high thermal gradients near the medical device and thus the temperature maxima. Exceeding the boiling temperature can therefore be completely invisible from the operator's point of view, leading to both a risk of tissue perforation for the patient and a modification of the local magnetic field which invalidates the temperature measurement in up to more than 40% of clinical cases [12–14].

In light of these limitations, numerical heat transfer simulations represent a powerful alternative to complement MRI thermometry. They can incorporate important physiological factors, such as vascular blood flow [15], temperature-dependent tissue properties [16], blood perfusion [17], and metabolic heat generation [18], to improve temperature field estimation, help predict the size and shape of the ablated region and support treatment planning by identifying appropriate energy levels to avoid under-treatment or overheating [19,20]. Several high-fidelity models have been developed for LITT [21–24], RFA [25,26], and MWA [27,28]. However, their use in clinical practice remains limited, as adapting them to real-time conditions is still a major challenge. This highlights the need for thermal models that are not only accurate but also computationally efficient enough for real-time integration.

Accordingly, several studies have proposed analytical temperature solutions to the bioheat equation, such as steady-state formulations accounting for heat sink effects [29], Bessel function-based models exploring probe geometries and boundary conditions [30], or multi-tumor scenarios treated via Green's functions [31], others have also introduced approximations using porous media theory to describe tissue and blood temperature distributions [32]. However, these studies largely focus on theoretical derivations and source term approximations without targeting experimental application or validation.

Building on these limitations, the core innovation of this study is the development of a computationally efficient thermal model based on a novel analytical formulation, designed to recover critical temperature features while remaining computationally efficient. The proposed framework is fully analytical for LITT and RFA and employs a hybrid formulation in the Laplace domain for MWA, discretized only in space. This approach avoids time-stepping or iterative procedures, enabling the direct evaluation of temperature fields at arbitrary time points and supporting arbitrary applicator orientations in three-dimensional space. The formulation is therefore adaptable to realistic interventional conditions and compatible with the temporal resolution of MRI thermometry.

The model is calibrated using the temperature evolution extracted directly from MRI measurements in selected regions of interest, rather than relying on prior knowledge of the ablation device's exact parameters, which are often unavailable or uncertain in clinical settings. It aims to improve spatial resolution and recover critical details that may be lost or distorted, particularly in regions affected by artifacts or low signal quality. While the general concept of combining physics with data has been widely explored in the context of thermal ablation [33–38], our contribution is distinguished by this analytical formulation, which combines clinical adaptability with computational efficiency.

The remainder of this paper is organized as follows: Section 2 introduces the simplified thermal model, MRI thermometry protocol, and inverse calibration procedure; Section 3 presents the validation results; Section 4 discusses computational performance and methodological limitations; and Section 5 concludes by highlighting potential steps toward clinical application and continued refinement of the model.

2. Materials and methods

Figure 1 shows an overview of the method that is used to perform simulations of thermal ablation procedures, from the data acquisition up to the optimization process. For each step of the optimization method, the corresponding sections in this article are specified. The accuracy of the method was tested on a synthetic dataset of the MWA model. The methodology and results are available on Supplementary Material.

2.1. Simplified heat transfer model

The heat transfer model is based on Pennes bioheat equation [39], shown in Equation (1), assuming an initial spherical symmetry for the heat source. Since this assumption does not match the elongated geometry of the ablation device, we refine the model by representing the tip of the needle as a half-sphere and using the propagated circumference (equator) of the sphere to approximate the temperature distribution around the needle. This approach provides a practical representation of the thermal field while maintaining analytical tractability.

$$\frac{\partial T(r,t)}{\partial t} = \alpha_p \left(\frac{\partial^2 T(r,t)}{\partial r^2} + \frac{2}{r} \frac{\partial T(r,t)}{\partial r} \right) - C^* \omega_b \left(T(r,t) - T_b \right) + Q^*(r,t) \tag{1}$$

The thermal diffusivity is denoted α_p. $C^* = \frac{\rho_b C_b}{\rho C_p}$ where ρ, C_p, ρ_b, C_b denote, respectively, the density and specific heat of the tissue and the density and specific heat of the blood. T_b is the blood temperature and ω_b is the blood perfusion rate that are assumed to be constant. Finally $Q^*(r,t) = Q(r,t)/(\rho C_p)$ where $Q(r,t)$ is the heat source associated with the device used. In this equation, the dimensionless parameter C^* is close to one. Therefore, both parameters α_p and ω_b govern the heat transport within the medium. In addition, it must be mentioned that $\omega_b = 0$ in ex-vivo experiments.

We assume that the thermal diffusion depth during the process is far from the boundaries of the organ and is significantly smaller than the organ itself, thus minimizing boundary effects. Therefore, the medium is considered as a semi-infinite domain. The boundary conditions (BC) are expressed as:

$$BC_1 : T(r,t) \to \text{finite}, \text{at } r = 0, t > 0 \tag{2}$$

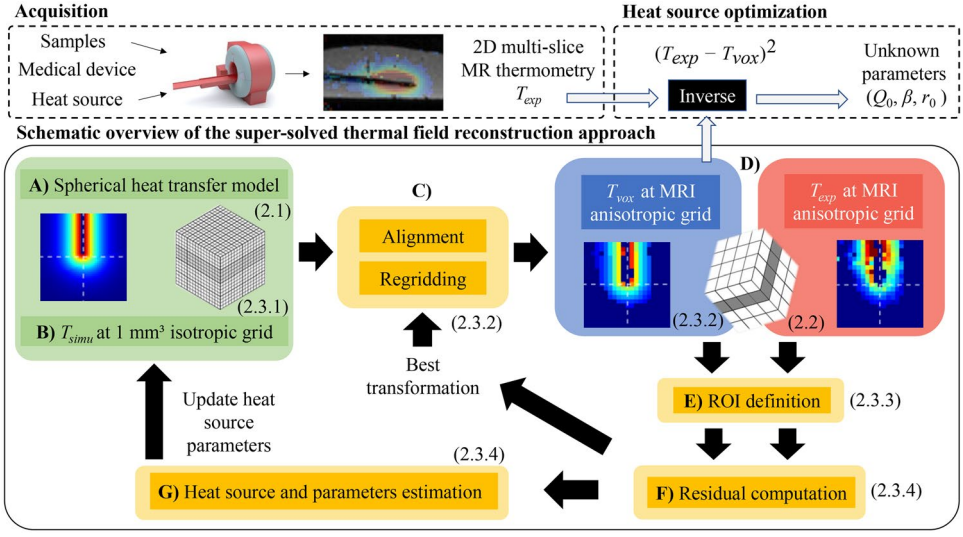

Figure 1. Schematic overview of the super-resolved thermal field reconstruction approach: The spherical heat transfer model is computed (A) and a half sphere is regridded in a 1-mm isotropic grid (B). The half sphere is then extended to form a cylinder. After estimation of the best rigid transformation (C), the simulated data is aligned and regridded to the MRI acquisition grid (D, in blue). ROI are defined (E) to compute the residual between simulated and experimental data (F). Finally, the estimated parameters are updated (G). For each step of the optimization method, the corresponding sections in the article are specified.

$$BC_2: T(r,t) = T_b, \text{ at } r \to \infty, t > 0 \tag{3}$$

And the initial condition (IC) is:

$$IC: T(r,t) = T_b, \text{ for } 0 \le r < \infty, t = 0 \tag{4}$$

If the medium is optically thick, solving the radiative heat equation shows that the laser absorption within the medium in the LITT process can be described as a Beer law where β denotes the absorption parameter as:

$$\text{LITT: } Q(r,t) = Q_0(t)\exp(-\beta r) \tag{5}$$

On the other hand, solving the Helmholtz equation in spherical 1D for the MW process leads to the expression of the heat source as:

$$\text{MWA: } Q(r,t) = Q_0(t)\exp\left(-\beta\sqrt{r}\right) \tag{6}$$

Finally, the heat source can be assumed uniform in a r_0 radius sphere for the RF process as:

$$\text{RFA: } Q(r,t) = Q_0(t)\,H(r - r_0) \tag{7}$$

where H denotes the Heaviside function. In order to calculate the temperature whatever the transient behavior of the source it is considered $Q_0(t) = \delta(t)$ in Equations (5), (6) or (7), meaning that the impulse response $h(r,t)$ is calculated from relations (1) to (4). Finally, based on the linearity assumption, the temperature field is calculated using the convolution between the impulse response and the source as:

$$T'(r,t) = T(r,t) - T_b = \int_0^\infty h(t-\tau)Q_0(\tau)\mathrm{d}\tau \tag{8}$$

Considering the three configurations, analytical and hybrid solutions of Equations (1)–(4) are derived as reported in the appendix. Those solutions are based on the use of a variable change for the spatial coordinate and the use of the Laplace transform on functions depending on time. The hybrid approach involves the use of the Laplace transform and of finite-difference techniques and can be generalized to all three energy modalities. The inverse Laplace transform is performed using Stehfest's algorithm [40]. The convolution product is performed using the fast Fourier transform. These solutions are finally used to express the temperature $T(r,t)$ as a function of radial distance r and time t.

Although the bioheat equation is solved under the assumption of a semi-infinite medium, this is adopted solely for mathematical simplification and computational efficiency. In practice, both the physical and computational domains are finite, and the Dirichlet boundary condition $T(r \to \infty, t) = T_b$ is applied at the outer edge of a domain large enough (50 mm) to ensure negligible boundary effects. This assumption is justified when the thermal diffusion length during the procedure remains smaller than the physical extent of the medium. The boundary condition at $r = 0$ is a classical condition in spherical or cylindrical coordinates and simply enforces finite temperature at the center, as established in foundational heat transfer literature [41,42].

2.2. MRI thermometry

MRI thermometry is performed using the Proton Resonance Frequency Shift (PRFS) method that computes the temperature change ΔT from the difference between a given phase image $P(t)$ acquired during treatment and a reference phase image $P(t_{ref})$ acquired prior to heating [43]. The temperature change ΔT is given by:

$$\Delta T = \frac{P(t) - P(t_{ref})}{\sigma\gamma T_E B_0} \tag{9}$$

where γ is the gyromagnetic ratio of hydrogen ($\approx 2\pi \times 42.58$ MHz T^{-1}), $\sigma = -0.0094$ ppm C^{-1} is the PRFS temperature coefficient [44], B_0 is the magnetic field strength (1.5 T here), and T_E is the echo time of the MR gradient echo sequence used for phase mapping.

Spatial-temporal drift correction and temporal filtering using a first-order low-pass Butterworth filter with a cutoff frequency of 0.14 Hz were applied based on this initial implementation [7]. Temperature uncertainty was approximated using the standard deviation of temperature (STD) computed in each pixel from all slices over the first dynamic acquisitions acquired before energy delivery. A mask was automatically created on each slice to exclude voxels with low signal-to-noise ratio (in the background or on the medical device for example). The mean and standard deviation of $\sigma(T)$ values were analyzed on a 15×15 ROI of voxels.

2.3. Mapping the analytical solutions on the experimental voxel network

Mapping analytical solutions onto an experimental voxel network involves a process of calculating the average temperature per voxel based on the analytical solution. This calculation can be performed directly on the MRI grid, provided that the device's exact position is known. In practice, however, this information is often unavailable or too imprecise. It is indeed challenging to determine the precise location of the needle on magnitude images of the echo planar imaging (EPI) sequence used for temperature monitoring. This is because the presence of a medical device results in a loss of signal in the surrounding area [45,46]. The artifact linked to the difference in susceptibility between the tissue and the device is all the greater the larger the echo time (TE) [47]. As an alternative, a 3D acquisition can be performed with an isotropic spatial resolution of 1 mm before the ablation. However, alignment with the EPI sequence and temperature maps is not guaranteed. This applies even to static objects as EPI sequences suffer from geometric distortions in the phase encoding direction [48,49]. In the vicinity of the device, and therefore the energy source, even a small positioning error will have a significant impact on the distribution of the temperature field, which does not vary linearly in space. Supplementary Figure 1 illustrates in 1D the impact of the partial volume and of the relative position between the medical device and MRI acquisition grid. Supplementary Figure 2 shows the impact on temperature in 2D of a shift in the position of the needle that is less than the size of a voxel. In practice, offset may occur in any direction. The relative tilt between the MRI grid and the device must also be considered, as there is no guarantee that the main axis of the medical device will match the MRI grid axes exactly. A procedure was designed to align the simulated temperature field with the experimental temperature field from MRI. This mapping is crucial to ensure that simulated and experimental temperature fields can be compared accurately. Calculations were performed on two systems: one laptop equipped with 12th Gen Intel® Core™ i7-12700H × 20, 64 GB RAM and one server equipped with Intel® Xeon(R) Gold 6248 R CPU @ 3.00 GHz × 96, 881 GB RAM.

2.3.1. Voxel-Averaged temperature calculation

The first step in this process is to calculate the voxel-averaged temperature based on analytical or hybrid solutions. A simulated rectangular grid at 1 mm isotropic resolution is constructed to generate a voxel grid representation. For each index on this simulated grid, the radial distance r is calculated to match the spatial location of the corresponding voxel. The temperature for each voxel is then averaged by integrating over the radial bounds that the voxel represents, ensuring that the continuous temperature field is accurately captured within each discrete voxel. For each voxel, the average temperature $T_{vox}(X,Y,Z,t)$ is calculated as:

$$T_{vox}(X,Y,Z,t) = \frac{1}{\Delta r}\int_{r}^{r+\Delta r} T'(r,t)\, r\, dr \tag{10}$$

where $T'(r,t)$ is the temperature as described in Equation (8) and Δr represents the radial length of the voxel. Thus, taking advantage of the spherical symmetry condition, the process is repeated in other directions until a hemisphere is formed. A complete sphere would not account for the length of the ablation, which has a more elongated shape. Therefore, to make the geometry more representative of

Table 1. Thermal properties used in temperature calculations.

	MWA	LITT and RFA
	Bovine liver	Agar-gel
Thermal conductivity, k ($Wm^{-1}K^{-1}$)	0.5 [50]	0.6 [51]
Volumetric heat capacity, ρc_p ($Jm^{-3}K^{-1}$)	3,740,000 [50]	4,133,000
Thermal diffusivity, α ($m^2 s^{-1}$)	1.34×10^{-7}	1.45×10^{-7} [52]

Table presenting the thermal properties considered for each energy source, with bovine liver data applied for MWA and agar-gel for RFA and LITT.

the process, the central circumference is repeated and added to the hemisphere, giving the simulation an elongated cylindrical shape. Thermal properties used for the temperature solution are presented in Table 1.

Temperature is calculated along the radial direction in 0.1 mm steps, then mapped onto a 3D Cartesian grid of $50\times50\times50$ voxels with 1 mm resolution. This discretization ensures compatibility with the MRI image resolution and allows efficient interpolation. The temporal discretization follows the same time steps as the MRI acquisition for each energy, covering both heating and post-heating phases. Cooling effects are naturally captured through convolution with the time-dependent heat source. Thanks to the Laplace transform, the time step can be chosen at any value and matches those of the MRI acquisition in each case without risk of divergence of the numerical scheme.

2.3.2. Alignment of simulated and experimental temperature fields

The next step involves aligning this simulated 4D temperature field with the experimental temperature field obtained from MRI. This registration is performed using ANTs [53] that estimates and applies the resulting rigid transformation matrix to the target image (simulated temperature field). This produces a new version of this target image that aligns spatially with the reference image (MRI measurements), preserving its internal geometry and relative distances.

2.3.3. Masking procedure

To ensure that source estimations are based on accurate data, regions of interest (ROI) are created for both simulated and experimental data. Only simulated voxels with a mean temperature change greater than 3 C during the course of the ablation were included in the spatial averaging. It ensures that only voxels with significant temperature change contribute to the heat source identification. Only experimental voxels with a standard deviation of temperature lower than 3 C before the course of the ablation were used. It excludes measurements that may have suffered from insufficient signal-to-noise ratio, particularly near the medical device. The union of the two ROIs is then used in further process.

2.3.4. Heat source identification and parameters estimation

In the proposed models, the heat sources are parameterized by $Q_0(t)$ and β for MWA and LITT, and by $Q_0(t)$ and r_0 for RFA. The objective, therefore, is to estimate the unknown parameters by minimizing the discrepancy between the simulated and measured temperatures. This estimation can be performed globally considering the entire time range, from the initial time t_{start} up to the final time t_{end} of the thermal ablation process. To achieve this, an objective function S is defined as the sum, over all voxel coordinates (X,Y,Z) and time t, of the quadratic difference between measured temperatures T_{exp}, and simulated temperatures T_{vox}, as:

$$S=\sum_{X,Y,Z}\sum_{t=t_{\text{start}}}^{t_{\text{end}}}\left(T_{\text{exp}}(X,Y,Z,t)-T_{vox}(p(t),X,Y,Z,t)\right)^2 \tag{11}$$

Where $p(t)=(Q_0(t),\beta)$ for MWA and LITT and $p(t)=(Q_0(t),r_0)$ for RFA is the unknown parameters. The minimization algorithm is the Trust Reflective Region algorithm [54].

It is important to note that T_{vox} corresponds to a voxel-averaged version of $T'(r,t)$, as defined in Equation (10), and therefore represents the temperature variation relative to the initial state rather than the absolute temperature. Similarly, T_{exp} corresponds to the temperature difference estimated by MRI

thermometry based on the PRFS method, as given in Equation (9). They are therefore both relative temperature values.

2.3.5. Error metrics

The accuracy of the reconstructed temperature fields was assessed using the root mean square error (RMSE) and the normalized root mean square error (NRMSE). The RMSE, expressed in degrees Celsius, quantifies the voxel-wise difference between the simulated (T_{vox}) and experimental (T_{exp}) temperatures over all dynamic acquisitions during the heating phase:

$$\mathrm{RMSE}(T_{vox}, T_{exp}) = \sqrt{\frac{1}{N}\sum_{i=1}^{N}\left(T_{vox,i} - T_{exp,i}\right)^2} \tag{12}$$

where N is the number of repetitions.

To provide a dimensionless metric, we also compute the NRMSE by normalizing the RMSE with the experimental temperature range:

$$\mathrm{NRMSE}(T_{vox}, T_{exp}) = \frac{\mathrm{RMSE}(T_{vox}, T_{exp})}{T_{exp,max} - T_{exp,min}} \tag{13}$$

where $T_{exp,max}$ and $T_{exp,min}$ are the maximum and minimum experimental temperatures observed during heating.

2.4. Experimental procedure

The ablation protocol including MWA, RFA and LITT and associated detailed sequence parameters are listed as follows.

2.4.1. Microwave ablation

An AveCure microwave system (MedWave, San Diego, USA) was used to perform the ablation using a 14-gauge large antenna inserted percutaneously under MRI guidance. The device was connected to a generator located outside the Faraday cage using a shielded cable provided by the manufacturer. Ablation duration was set to 7 min 30 with a target temperature of 60°C on a cow liver at room temperature. A delay of 30 s was observed before starting the energy deposition. MR temperature images were obtained on a 1.5 T clinical MRI (Magnetom Sola Fit, Siemens Healthineers) using a multi-slice multi-shot EPI sequence positioned parallel to the MW probe. A stack of 13 slices was acquired dynamically every 4 s using the following parameters: TE = 19 ms, TR = 47.29 ms, FA = 90°, FOV was 300 mm × 300 mm, matrix size = 128 × 128, in plane spacing = 2.34375 mm × 2.34375 mm, slice thickness = 3 mm, slice gap = 1.5 mm, bandwidth/pixel = 953 Hz, GRAPPA acceleration factor = 2, repetitions = 190.

2.4.2. Laser induced thermal ablation

The prototype laser device (ALPhANOV, France) is composed of a laser diode source (976 nm wavelength, maximum output power of 27 W) connected to a 240 µm multi-mode optical fiber ended with a glass diffuser tip (1 cm long, 1.8 mm diameter). Full description of the device is available [55]. The spatial distribution of the heating produced by the laser was obtained by heating a gel phantom at 8 W for 1 min under MR thermometry. The 3% Agar-gel phantom is in a cylindrical container. A delay of 60 s was observed before starting the energy deposition. MR temperature images were obtained on a 1.5 T clinical MRI (Avanto, Siemens Healthineers) using a multi-slice single-shot echo planar imaging sequence positioned perpendicular to the laser probe. A stack of 8 slices was acquired dynamically every 2s using the following parameters: TE = 21 ms, TR = 2000 ms, FA = 40°, FOV was 158 mm × 158 mm, matrix size = 128 × 128 in plane spacing = 1.234375 mm × 2.34375 mm, slice thickness = 3 mm, no slice gap, bandwidth/pixel = 1445 Hz, GRAPPA acceleration = 2, partial Fourier = 6/8, repetitions = 250.

2.4.3. Radio-frequency ablation

An MR compatible RFA catheter (Vision-MR Ablation Catheter, Imricor Medical Systems, Burnsville, MN, USA) with two embedded micro-coils (proximal and distal) was used to perform the ablation. The catheter was connected to a clinical RF cardiac ablation generator (Irvine Biomedical, Inc, 1500T11) located inside the Faraday cage, using the Advantage MR system (Imricor Medical Systems, Burnsville, MN, USA). Ablation duration was set to 30 s with a power at 5/10/15/20 W on an agar gel. A delay of 30 s was observed before starting the energy deposition. MR temperature images were obtained on a 1.5 T clinical MRI (Aera, Siemens Healthineers) using a multi-slice multi-shot echo planar imaging (EPI) sequence positioned parallel to the MW probe. A stack of 8 slices was acquired dynamically every 1 s using the following parameters: TE = 28 ms, TR = 930 ms, FA = 60°, FOV was 170 mm × 170 mm, matrix size = 148 × 148, in plane spacing = 1.14 mm × 1.14 mm, slice thickness = 3 mm, slice gap = 0.3 mm, bandwidth/pixel = 1165 Hz, GRAPPA acceleration factor = 2, repetitions = 150.

The number of repetitions refers to the number of consecutive acquisitions of 3D MRI volumes. The time interval between the acquisition of two consecutive 3D MRI volumes, typically is defined by the repetition time (TR) of the thermometry sequence. This value corresponds to the temporal resolution or (frame update) of the temperature measurements. While in some cases it matches the minimum acquisition time of the sequence, in practice it may include additional dead time depending on the experimental setup and MRI parameters. These values are also displayed on Table 2.

3. Results

Table 2 shows the computing times for each simulation for the two used systems. The time required to calculate the solution at the averaged voxel temperature was 6.93 ± 1.57 s for all datasets. The time required to align the simulated data with the experimental data until the residual was 23.9 ± 2.11 s for all datasets on the server. Relative to the number of repetition steps, the time to simulate the model is less than 37 ms and the time to align the data is less than 140 ms. Optimization of the heat flux parameters requires between 50 and 200 iterations to converge, i.e. between 1h and 6h depending on the datasets. Results of the estimation are presented in Table 3.

Supplementary Figure 3 displays the temporal standard deviation of the temperature before the ablation for each acquisition. After heat source parameters have been optimized, a comparison between simulated and experimental MWA maps are shown in Figure 2 after realignment and regridding at MRI resolution. The spatial distribution of temperature is shown at repetition 120 close to the tip of the MW needle (Figure 2a). Simulated data (Figure 2b) were aligned on experimental data (Figure 2c). A more precise representation of the thermal field is provided by the refined simulation on a 1 mm isotropic grid (Figure 2d). The maximum temperature increases ΔT_{exp}^{max}, ΔT_{vox}^{max}, and ΔT_{simu}^{max} were 52, 46, and 51 °C, respectively.

Table 2. Computational time comparison for temperature field processing.

	MWA	LITT	RFA
Number of repetitions	190	250	150
Frame update (s)	3.75	2.00	1.00
Measurement time (s)	712.5	500	150
	Server Intel Xeon Gold 6248 R @3.00 GHz × 96 threads, 881.1 GiB RAM Ubuntu 20.04.5 LTS		
Simulation (s)	6.6	9.0	5.2
Alignment (s)	26.2	24.4	21.1
Total (s)	32.8	33.4	26.3
Total per rep. (s)	0.17	0.13	0.18
Dead time (s)	679.7	466.6	123.7
	Laptop Dell Inc. Precision 5570 12th Gen Intel Core i7-12700H 20 threads, 64.0 GiB RAM, Ubuntu 22.04.5 LTS		
Simulation (s)	12.7	14.9	9.1
Alignment (s)	45.2	39.6	33.4
Total (s)	57.8	54.4	42.5
Total per rep. (s)	0.30	0.22	0.28
Dead time (s)	654.7	445.6	107.5

Summary of experimental acquisition parameters and computation times (alignment and simulation) performed on two different processors for the hybrid formulation.

Table 3. Estimated heat flux parameters from temperature field comparison.

	Q_0 (Wm^{-3})	β	r_0 (m)
MWA	4.20×10^8	72 ($m^{-1/2}$)	—
LITT	2.45×10^7	950 (m^{-1})	—
RFA	4.70×10^6	—	0.014

Table displaying the optimized heat flux parameters that minimize differences between simulated and MRI-measured temperature fields.

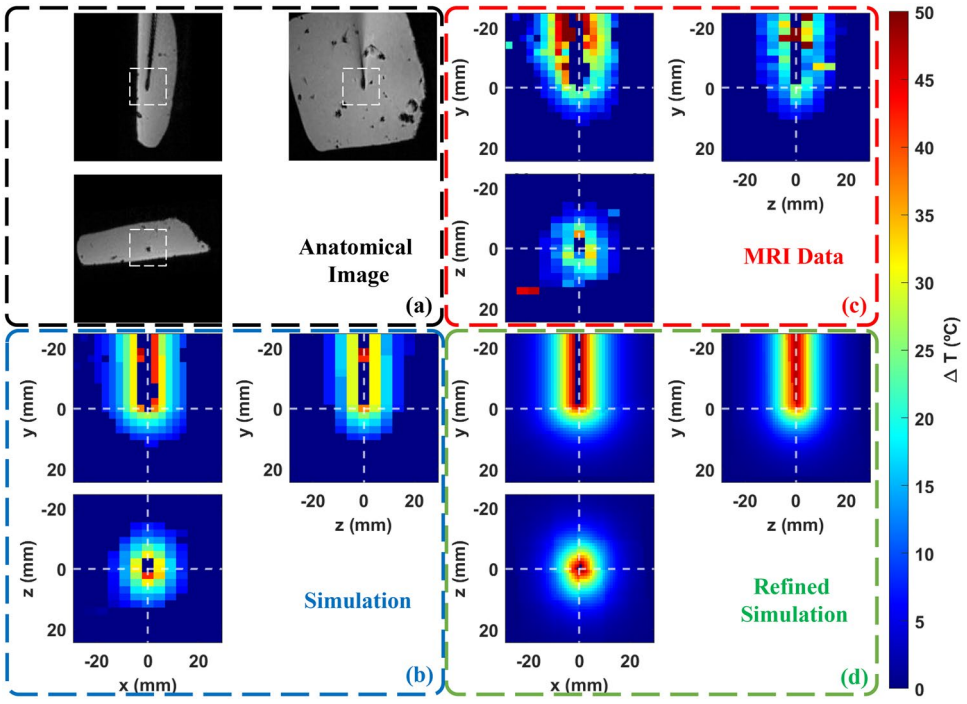

Figure 2. Comparison between simulated and experimental temperature maps for the MWA in *ex vivo* liver. T1-weighted anatomical images close to the tip of the MW needle (indicated by white dotted outline) are shown in top left corner (a) using three orthogonal views. Other panels show (using the same representation) the experimental temperature data (c), the simulation aligned and regridded to the MRI acquisition grid (b) and the super-resolved simulation at 1 mm isotropic resolution (d). Note that all displayed temperature fields have been masked using the ROI definition in Section (2.3.3). Voxels on the needle are masked because their SNR is insufficient, while external voxels are masked because the temperature rise is minimal. Note also that the resolution of the in-plane view ($2.3\times2.3\,mm^2$) differs from the resolution of the two other orthogonal views ($2.3\times3.0\,mm^2$).

Figure 3 presents the temperature comparison as a function of time. A 5×5 voxel kernel was selected near the ablation site, and the root mean squared error was computed across the entire MRI grid. The maximum observed temperature variation was +40 °C for both simulated and experimental data. Increased noise is noticeable in the vicinity of the device. Nonetheless, considering the RMSE field of view for MWA ($21\times21\times13$ voxels, $\approx$5000 voxels), 83.7% of the voxels showed an RMSE $\leq$ 1°C, and only 0.5% exceeded 10°C, with a maximum value of 20°C. Accordingly, the maximum NRMSE reported was 0.43.

Figure 4 compares the temperature profiles of experimental data (red) with simulated data mapped on the MRI grid (blue, referred to as 'without refinement') and with the full-resolution simulation on the 1 mm grid (green, referred to as 'with refinement'), during both heating and cooling periods. In line 2, the maximum temperatures ΔT^{max}_{exp}, ΔT^{max}_{vox}, and ΔT^{max}_{simu} were 38°C, 35°C, and 49°C, respectively, at repetition 120. In both lines 1 and 2, the refined simulation overestimated the experimental temperature during the heating period (repetition 120) by 17°C and 11°C, respectively, while underestimating it during the cooling period (repetition 180) by 15°C and 8°C, respectively.

Following the same approach, Figure 5 presents a comparison between simulated and experimental temperature maps for LITT, after applying the same realignment and regridding steps. The temperature

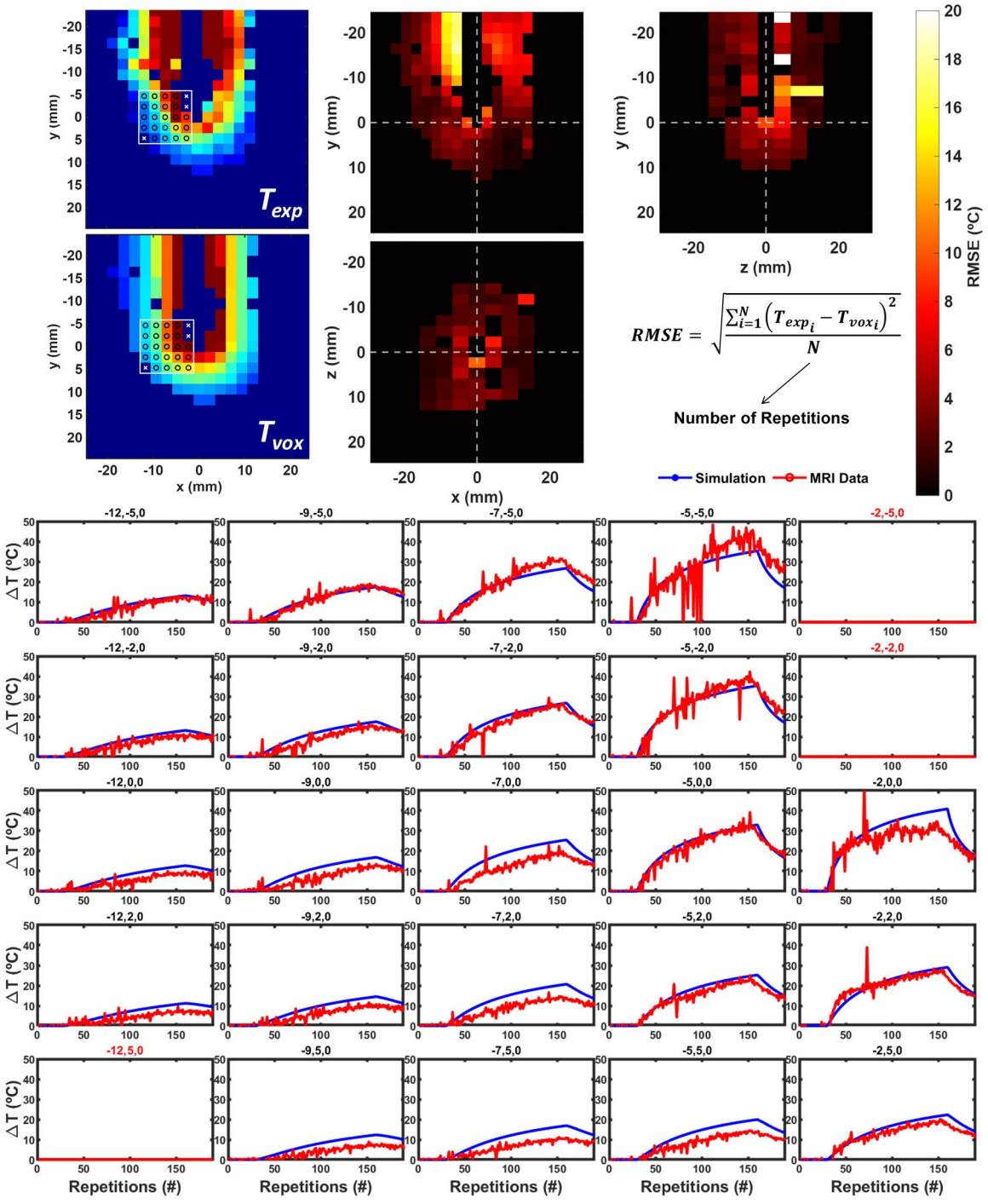

Figure 3. Representative case of temporal temperature variations during MWA. (Top left) Simulated and experimental temperature maps at the MRI acquisition grid near the needle tip are shown in one slice at dynamic acquisition #120. (Top right) Three orthogonal views display the RMSE values for a region near the applicator, alongside its explicit mathematical formulation. RMSE is computed as the square root of the sum of the squared differences between experimental (T_{exp}) and simulated (T_{vox}) temperatures over time, normalized by the number of temporal repetitions. (Bottom) The temperature evolution as a function of dynamic acquisition is presented for a 5×5 voxel kernel, with simulated and experimental data shown in blue and red, respectively. The kernel's location is indicated on the temperature map, and some voxels have been masked based on the ROI definition in Section (2.3.3).

distribution near the optical fiber tip at repetition 100 is shown in Figure 5. The peak temperature increases recorded experimentally (Figure 5b), in the voxel-based data (Figure 5c), and in the simulation (Figure 5d) were 27°C, 22°C, and 27°C, respectively.

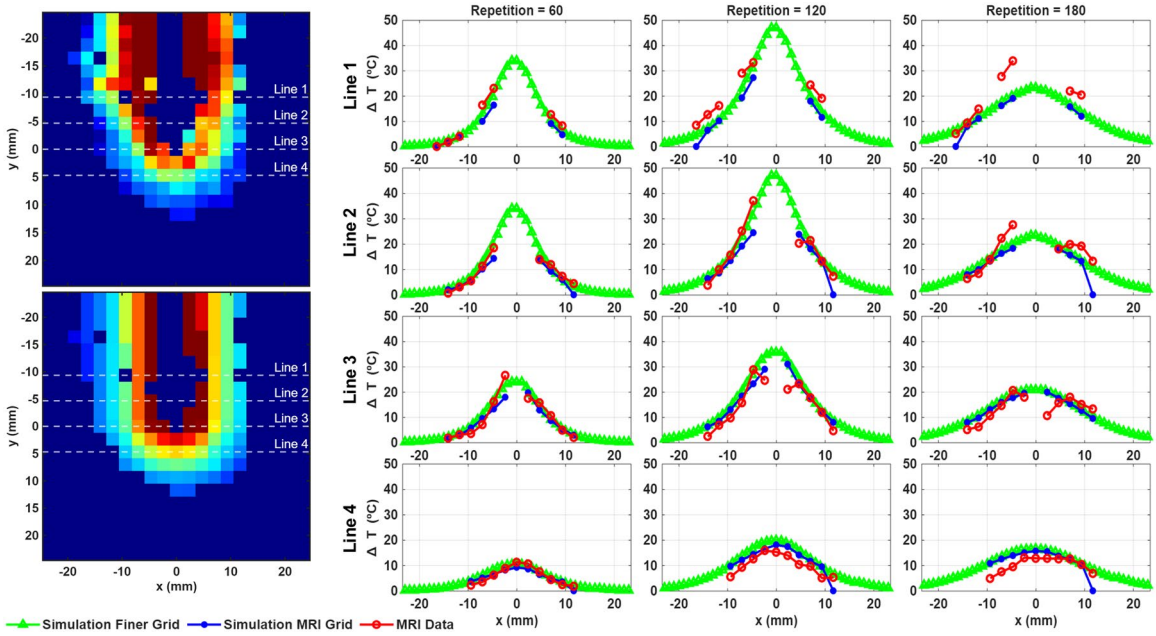

Figure 4. Comparison of temperature distributions along the ablation width during MWA. (Left) Simulated and experimental temperature maps at the MRI acquisition grid near the needle tip, with four lines indicating specific locations along the ablation width (x-axis). (Right) Temperature profiles along this dimension are shown for each of the four indicated locations at acquisitions #60 and #120 (heating phase) and #180 (cooling phase). Simulated temperatures at the MRI grid are displayed in blue, measured temperatures in red, and temperatures from the super-resolved solution with a $1\times1\times1\,mm^3$ grid in green. Some voxels have been masked based on the ROI definition in Section (2.3.3).

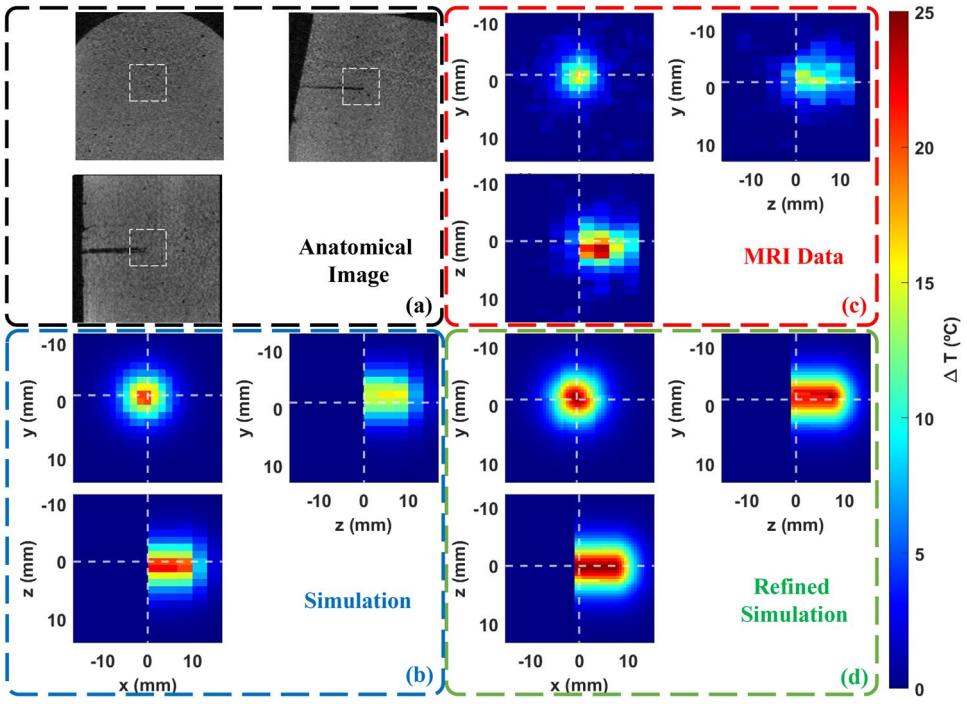

Figure 5. Comparison between simulated and experimental temperature maps for LITT in agar-gel. T1-weighted anatomical images close to the tip of the MW needle (indicated by white dotted outline) are shown in top left corner (a) using three orthogonal views. Other panels display, using the same representation, the experimental temperature data (c), the simulation aligned and regridded to the MRI acquisition grid (b), and the super-resolved simulation at 1 mm isotropic resolution (d). All temperature maps have been masked using the ROI definition in Section (2.3.3). Voxels on the applicator are masked due to insufficient SNR, while external voxels are masked due to minimal temperature rise. Note that the resolution of the in-plane view ($1.2\times2.3\,mm^2$) differs from the resolution of the two other orthogonal views ($1.2\times3.0\,mm^2$) and ($2.3\times3.0\,mm^2$).

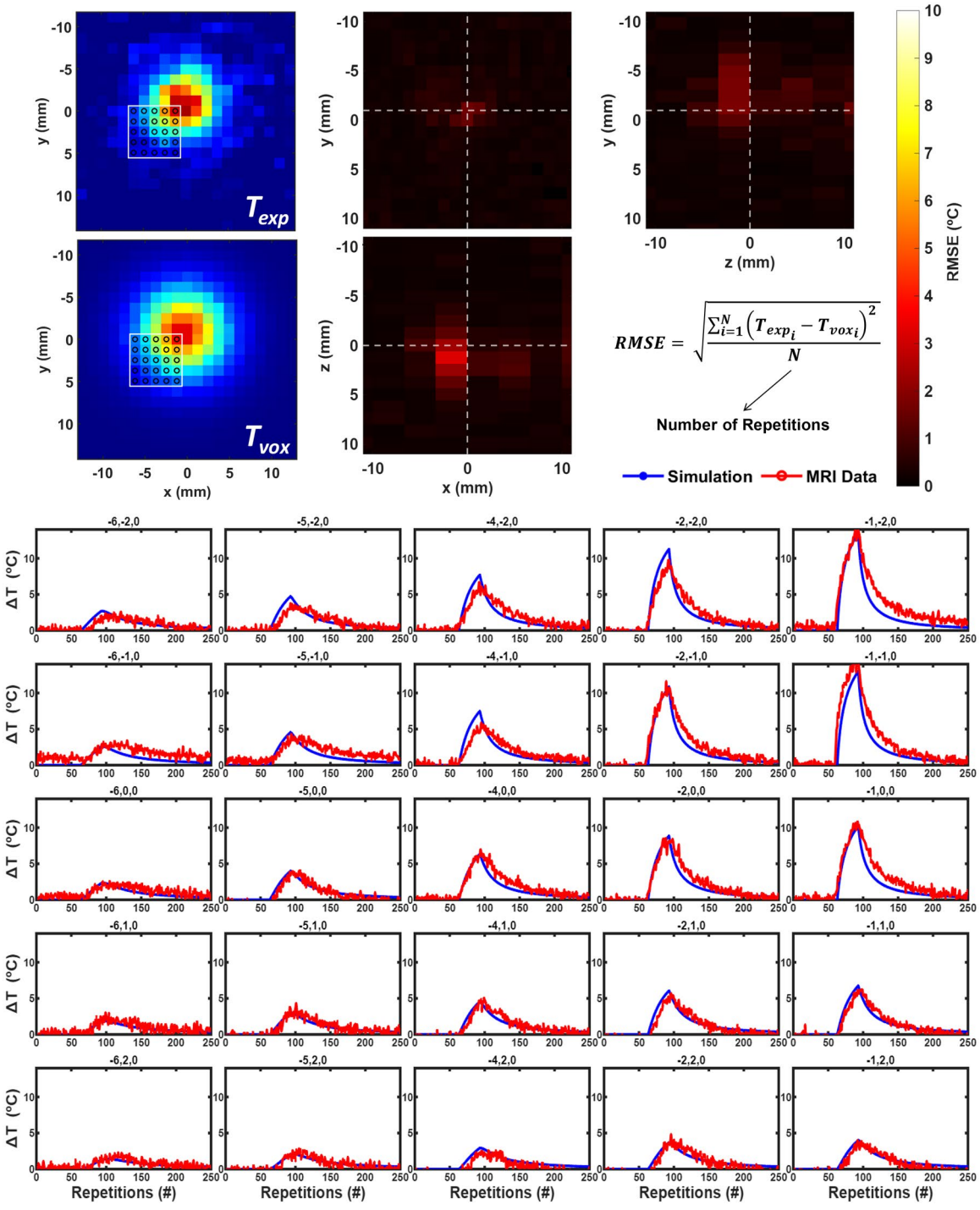

Figure 6. Representative case of temporal temperature variations during LITT. (Top left) Simulated and experimental temperature maps at the MRI acquisition grid near the applicator are shown in one slice at dynamic acquisition #100. (Top right) Three orthogonal views display the RMSE values for a region near the applicator, alongside its explicit mathematical formulation. RMSE is computed as the square root of the sum of the squared differences between experimental (T_{exp}) and simulated (T_{vox}) temperatures over time, normalized by the number of temporal repetitions. (Bottom) The temperature evolution as a function of dynamic acquisition is presented for a 5×5 voxel kernel, with simulated and experimental data shown in blue and red, respectively. The kernel's location is indicated on the temperature map, and some voxels have been masked based on the ROI definition in Section (2.3.3).

The temporal temperature evolution for LITT is shown in Figure 6. The largest temperature variation observed was +15°C. Considering the RMSE field of view (21 × 21 × 10 voxels, ≈4000 voxels), the agreement was particularly high, with 98.5% of voxels below 1°C and none above 5°C. The maximum reported NRMSE was 0.12.

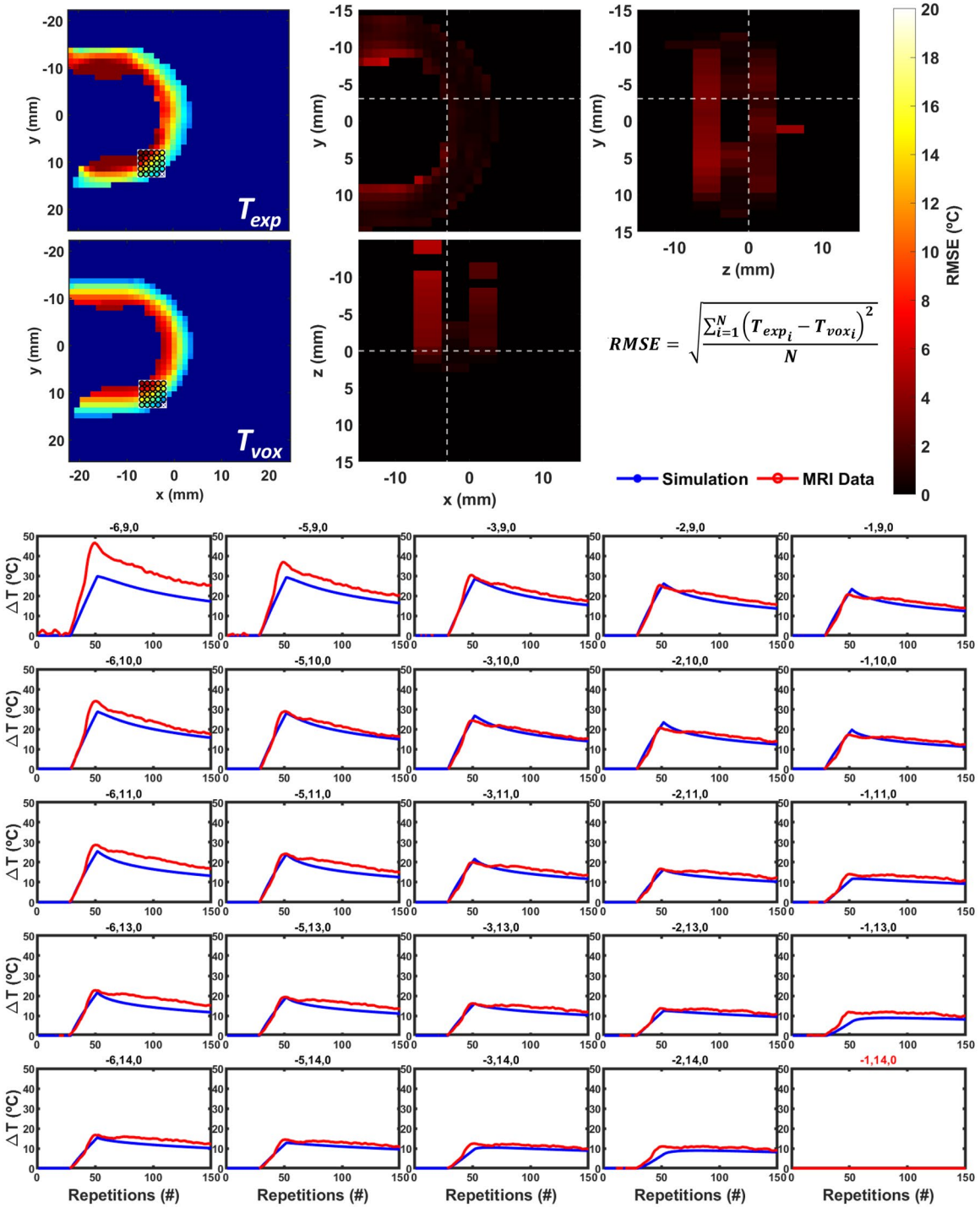

Figure 7. Representative case of temporal temperature variations during RFA. (Top left) Simulated and experimental temperature maps at the MRI acquisition grid near the applicator are shown in one slice at dynamic acquisition #70. (Top right) Three orthogonal views display the RMSE values for a region near the applicator, alongside its explicit mathematical formulation. RMSE is computed as the square root of the sum of the squared differences between experimental (T_{exp}) and simulated (T_{vox}) temperatures over time, normalized by the number of temporal repetitions. (Bottom) The temperature evolution as a function of dynamic acquisition is presented for a 5×5 voxel kernel, with simulated and experimental data shown in blue and red, respectively. The kernel's location is indicated on the temperature map, and some voxels have been masked based on the ROI definition in Section (2.3.3).

Similarly, the temperature evolution over time for the RFA procedure is presented in Figure 7. In this case, the maximum observed temperature variation was +40°C. For RFA (41 × 41 × 8 voxels), 93.7% of the voxels were within the lowest error range (≤1°C), with none above 10°C. The maximum NRMSE was 0.21.

4. Discussion

Our study, conducted at 1.5T using a multi-slice EPI sequence, evaluates the potential of a novel analytical and hybrid solution to the bioheat equation, enhancing temperature resolution at the subvoxel level. The proposed solution was tested against three different energy sources during *ex vivo* or phantom ablations. For each, by mapping the simulated temperature fields onto experimental data, we validate the model and confirm the accuracy of our approach.

Figures 2–4 present the results for MWA, conducted on an *ex vivo* bovine liver sample. The hybrid model developed in this study effectively represents the temperature distribution during the procedure. While some visual differences between the calculated and measured temperatures on the MRI grid are observed, they are expected given the simplified nature of the model. In Figure 4 the difference between the refined simulation and the interpolated field is due to spatial resolution: the green curve captures localized thermal peaks near the applicator thanks to the finer computational grid, whereas the blue curve corresponds to the interpolated version mapped onto the coarser MRI voxel grid, which smooths sharp temperature gradients.

Similarly, Figures 5 and 6 present the results for LITT, while Figure 7 shows the results for RFA, both performed on agar-gel phantoms. These procedures exhibit challenges similar to those encountered in MWA, though to varying degrees. In the case of LITT, the calculated temperatures show an exceptionally strong agreement with the MRI measurements, as evidenced by the remarkably low RMSE values. Even in regions near the applicator, where measurement noise is typically more pronounced due to previously discussed factors, the discrepancies remain minimal. This is largely attributed to the applicator design, which consists of an optical fiber ending in a glass diffuser tip, significantly reducing artifacts and minimizing interference in temperature measurements.

Differently, for RFA the influence of the applicator is more pronounced. The presence of a large region of 'blind voxels' is notable, resulting from the catheter dimensions and material properties, which introduce significant MRI artifacts and obscure temperature readings. Despite these challenges, the model successfully captures the overall thermal behavior, with a computation time slightly exceeding one minute and consistently low error levels.

In terms of quantitative performance, the maximum NRMSE values obtained reveal modality-dependent differences. LITT exhibits the lowest NRMSE, indicating that the model reproduces the heating dynamics relatively well in this configuration, which is consistent with the more localized and symmetric energy deposition characteristic of this modality. RFA shows an intermediate NRMSE, reflecting a satisfactory overall agreement, although pointwise deviations remain due to the complex electrode–tissue interactions that the simplified source model cannot fully capture. MWA presents the highest NRMSE, highlighting the challenge of representing the strong spatial heterogeneities of the electromagnetic field with a reduced thermal source.

As shown in Supplementary Figure 4, scatter plots of simulated versus experimental temperatures reveal that deviations are largely symmetrically distributed around the identity line, suggesting that errors are spread evenly rather than concentrated in specific regions. Correlation coefficients are high across all modalities ($r = 0.84$–0.91), and regression slopes are generally below unity, indicating slight systematic underestimation, with LITT showing the slope closest to 1.

It is important to emphasize that these values are derived within an approximative modeling framework, including idealized geometry, simplified heat source representations, and inherent limitations of MRI thermometry. Despite these simplifications and the inherent experimental noise, the NRMSE values remain well below unity, confirming that the model, while not exact, provides a reliable and computationally efficient approximation of the temperature evolution during thermal ablation. LITT, in particular, achieves the closest agreement, whereas RFA and MWA maintain reasonable fidelity at the global pattern level, illustrating the expected tradeoffs between model simplicity, experimental variability, and point wise accuracy. A more detailed discussion about limitations of this work and their implications is provided in the following sections.

4.1. Computation time

As presented in Table 2, the total computing times were carefully broken down to distinguish between simulation, data alignment, and parameter estimation. For each repetition the model requires

approximately 37 ms to simulate the average temperature field over the 3D grid, and 140 ms to align and regrid the simulated output to the experimental data. These values, obtained using parallel processing on a high-performance server (similar to those deployed on MRI scanner), demonstrate that both simulation and alignment steps together require less than 0.2 s per acquisition, which is considerably faster than the MRI repetition interval. This means that after each MRI scan, a 'dead time' could potentially be exploited to perform additional calculations, such as the real-time adjustment or estimation of the heat source parameters.

In a clinical setting, medical devices are typically operated within a certified range (as defined by CE or FDA standards), and MR acquisition protocols are also standardized, allowing the development of device-specific or patient-specific prior models. In practice, once a few representative cases are processed and the model is calibrated for specific devices and energy ranges, several parameters can be fixed or constrained, significantly reducing the dimensionality of the optimization problem. Therefore, although parameter estimation in this study was performed offline and took between 1 and 6 h depending on the dataset, this duration is mainly due to the chosen optimization algorithm and the absence of prior assumptions about device type or power level.

Compared to similar studies in the literature, our approach already demonstrates competitive performance. For instance [29], reported a simulation time of 35 s using analytical models for radiofrequency ablation at a similar spatial resolution (0.8 mm isotropic), but without including the alignment and remeshing steps required to match experimental data. Another work [56] relying on finite-difference models and recursive filters (e.g. Kalman filters) managed to perform real-time estimation, but only over highly reduced domains (1D or 2D grids with fewer than 125 data points). However, when comparing computational performance across studies on thermal ablation simulation, significant variability is observed depending on the model complexity, spatial resolution, and hardware utilization. For instance [57], reported real-time microwave simulations on a $20\times20\times20$ tetrahedral mesh, achieving a per-iteration computation time of only a few milliseconds using GPU acceleration with HLSL shaders, which translated into an overall speed-up of 55× relative to CPU execution [58]. simulated a 10-min radiofrequency ablation with 227,000 tetrahedral elements, requiring 3 to 6 min using a Tesla S1070 GPU accelerated with a Wavelet Algebraic Multigrid solver [59]., employing GPU-accelerated distance field approximations for interactive RF ablation planning on $\sim92\times92\times65$ voxel grids, achieved calculation times between 30 and 50 min for the complete ablation zone [60]. performed simulations for microwave therapy on an $85\times54\times85$ Yee cell domain, achieving 12 s per transmitter on a Tesla C2075, which could be reduced to ~1 s per transmitter with multi-GPU parallelization [61]. reported FEM-based RFA simulations with up to 1.5 million elements, requiring less than 3 min to predict a 26-min treatment protocol on a GPU [62]. further demonstrated the capability of a high-end Ampere A100 GPU to simulate a 5-min RFA procedure in under 2.5 s for 1.9 million tetrahedral elements.

In this context, our CPU-based model achieves simulation of the 3D temperature field in ~37 ms, and alignment plus regridding to experimental data in ~140 ms, for a total of ~0.2 s per acquisition, operating directly on a full $128\times128\times13$ voxel dataset (~210,000 voxels). Remarkably, these results were achieved without dedicated GPU hardware, relying solely on parallelized CPU computations. Although GPUs can accelerate larger meshes, our findings show that CPU-parallelized implementations can deliver competitive performance with modest hardware requirements and can be further improved through algorithmic refinements or partial GPU acceleration. While full real-time estimation has not yet been reached, the current framework is compatible with real-time simulation and offers a practical route toward fully real-time applications.

4.2. Limitations regarding heat source estimation

For the sake of simplicity, the results presented in Table 3 are based on a whole domain estimation, where the entire set of spatial and temporal information is used to estimate the unknown constant parameters. In this case, Q_0 and β for MWA and LITT, and Q_0 and r_0 for RFA. In the conducted experiments, there is no significant variation in the heat source, and the temperature changes are not large enough to affect β or r_0 over time. However, while this approach has been effective, it may not be the optimal one. In the case of linear models, parameter estimates can be updated progressively as new data

becomes available, eliminating the need for iterative procedures typically required in nonlinear optimization. This significantly reduces computational cost and improves efficiency, making sequential estimation a much faster alternative. Although it is not necessary for the current dataset, tests have demonstrated its effectiveness, and it is planned for future implementation, as the primary goal of developing both analytical and hybrid solutions is to minimize computational time. This would allow these methods to be seamlessly integrated into real-time identification procedures, further enhancing their practical applicability.

Another common limitation across all three procedures is the lack of optimization in determining the exact start and end times of the ablation, which can introduce minor temporal shifts in the temperature evolution. When accumulated, these shifts may contribute to slightly higher residual errors. However, this issue has already been identified, and improvements in time synchronization are planned for future updates of the method.

4.3. Limitations regarding nonlinear thermal behaviors

Also concerning the optimization procedure, in this work, we focus on estimating the heat source parameters rather than both the heat source and the thermal properties. It is assumed that the thermal properties are well-characterized by established literature values and do not vary significantly during the ablation procedure. This former assumption is quite strong since it means that the thermal properties of the biological medium will not vary according to either the temperature or the state (coagulated or not) of the affected zone. However, several experimental studies support that within the moderate temperature range used in our setup (up to 50°C). Ref. [63] reported approximately a 25% increase in thermal conductivity between 20°C and 80°C, with less than 15 % change up to 50°C, indicating that temperature dependence is a second-order effect in this regime. Ref. [64] further support that thermophysical properties remain constant up to 90°C, with variability mostly attributable to tissue heterogeneity and measurement methods. In this way, we consider that these variations can be neglected without sacrificing accuracy in favor of simplifying the model.

This simplification is also justified by the relatively lower sensitivity of the model output to thermal properties. Although they do affect the temperature distribution, their interference is minor, especially compared to power and ablation time [65]. This is further illustrated in Supplementary Figures 5 and 6, where a 20% variation in thermal diffusivity produces considerably smaller changes in temperature fields than similar variations in heat source parameters Q_0 and β. Additionally, factors such as electrical conductivity, cell death thresholds, and blood perfusion have been shown to be of greater importance than thermal properties in defining the ablation outcome, particularly regarding the extent of tissue necrosis [65–67]. However, these biological and electrical parameters are not explicitly included in the present study.

The inclusion of these factors would require more complex and computationally intensive models, often relying on detailed tissue-specific parameters that are difficult to measure or estimate *in vivo*. Blood perfusion, for example, varies spatially and temporally during ablation and can significantly alter heat dissipation, necessitating coupled bioheat transfer and perfusion models. Similarly, electrical conductivity and cell death thresholds involve nonlinear and dynamic processes that would complicate parameter estimation and potentially reduce model tractability. Given the primary objective of this work (to reconstruct temperature distributions based on MR thermometry data and estimate heat source parameters) the current model prioritizes simplicity and computational efficiency.

Nonetheless, we acknowledge that certain nonlinear thermal behaviors, such as the temperature dependence of tissue properties and the complex interaction between electromagnetic fields and tissue during MWA or RFA, become more prominent at higher temperatures. These effects are not captured under the experimental conditions used in this study, and this should be considered when extrapolating the results to clinical scenarios. However, when considering the overall performance of the model, the temperature range does not appear to be a dominant source of mismatch. Rather, a combination of factors, including experimental heterogeneity, MRI-related artifacts, model simplifications, and uncertainties in applicator positioning, more notably contribute to the observed discrepancies. Still, although further refinements are possible, the model remains a reliable and robust tool within the tested conditions, as demonstrated by the RMSE results.

Thus, by pre-calibrating or adopting literature values for thermal properties, our modeling can concentrate on accurately estimating the heat source parameters, which are critical for achieving the desired thermal dose and treatment outcome, without the additional computational burden of simultaneously identifying a parameter that is both less variable and less directly controlled during the procedure. The linear model also ensures that the two optimization processes (topological registration and source parameter identification) occur independently, without correlation or error propagation between them. Since no property depends on temperature, state or position, both optimizations can be performed without one parameter influencing the other.

Additionally, two of the estimated values in the optimization process can be verified. As the formulation of the heat source for LITT follows the Beer-Lambert law, β, in fact, represents the absorption coefficient of the medium (agar-gel in this case). This coefficient can also be calculated by the expression $\beta = \frac{4\pi\kappa}{\lambda}$, where κ is the extinction coefficient (the imaginary part of the refractive index of the material) and λ is the wavelength of incident light. Agar gels in general exhibit minimal absorption, with pure agar being nearly as transparent as water. If additional scattering or absorbing additives are introduced, the imaginary part of the refractive index may increase, but for pure agar gels, the extinction coefficient remains extremely low. In practical terms, for a 3% agar gel, κ is considered negligible compared to the real part of the refractive index having an extinction coefficient κ below 1×10^{-4} [68]. Considering a typical range for κ from 1×10^{-5} to 1×10^{-4}, the absorption coefficient at a wavelength of 976 nm is expected to be within the interval from $120\,m^{-1}$ to $1200\,m^{-1}$, including the estimated value of $950\,m^{-1}$. Furthermore, the estimated parameter r_0 in the RFA process represents the ablation radius. As a geometric parameter, it can be directly measured and validated by comparing it with the contours observed in Figure 7.

4.4. Limitations regarding the simplified geometry

A key limitation of the current model lies in its reliance on a simplified, symmetric geometry that assumes isotropic heat propagation. While this assumption captures the overall directional behavior of thermal propagation in standard ablation procedures, it becomes less accurate for systems with internal cooling, such as Cool-tip or bipolar/multipolar RF probes, where internal heat exchange significantly alters the thermal distribution. Asymmetrical thermal patterns can also arise in microwave ablation due to directional antennas, or in general for all modalities in the presence of anisotropic thermal conduction, particularly relevant in tissues such as the brain, or in the vicinity of large blood vessels, which can act as local heat sinks. These situations lead to strongly non-symmetric temperature fields that are not captured by the current model.

Although the model does not capture all geometric details of the ablation or compute temperatures at the applicator itself, it still provides a reliable estimation of the thermal field. Since the procedure is conducted in an agar-gel phantom, an isotropic medium, it aligns well with the simplifications of the model, further enhancing its accuracy. The presence of the applicator affects temperature measurements in two key ways. First, it introduces noise due to its metallic structure, which distorts the MRI signal and reduces the accuracy of the recorded temperatures in its immediate vicinity. Second, it obscures crucial information in voxels near the applicator, preventing direct measurement of temperature values in these regions. This can lead to localized discrepancies between the experimental data and the simulated results, particularly where thermal gradients are the steepest.

4.5. Limitations regarding perfusion effects

The analytical formulation used in this study is based on a simplified version of the bioheat equation, where perfusion is modeled as a spatially uniform term. Consequently, the model allows the inclusion of a global perfusion effect but does not support the explicit incorporation of spatially varying (local) perfusion. This limitation prevents the model from accounting for the cooling effects induced by individual blood vessels, which can significantly impact the shape and extent of the heated area, particularly in highly perfused tissues.

The perfusion, was not included in the current model during the experimental validation due to the *ex vivo* and phantom-based nature of the experiments, its incorporation remains an important step for future clinical applications. One possible direction is to reformulate the model to estimate heat flux at the voxel level, which could help identify vascularized regions and better account for local cooling effects. This would enhance temperature reconstruction *in vivo*, especially in heterogeneous and anisotropic tissues, without requiring explicit modeling of blood flow dynamics.

4.6. Limitations of the experimental validation

One last limitation of this study is that only a single acquisition was performed for each energy level. While this allowed us to demonstrate the feasibility and potential of the proposed analytical model across the three most commonly used energies in thermoablation, further experiments are needed to assess its robustness and accuracy in varied clinical scenarios and across multiple patients or sessions.

Also, relatively low power settings were used in the experiments compared to typical clinical ablation protocols. While therapeutic ablation procedures commonly operate at temperatures ranging from 60°C to 120°C depending on the organ and pathology, the experiments presented here were performed at lower energy levels, generally resulting in peak temperatures below 80°C. This choice was deliberate: when using agar gel phantoms, temperatures above 60°C can cause irreversible phase changes (melting), which not only alter the thermal properties of the medium but also introduce significant susceptibility artifacts in the MRI. Susceptibility artifacts also appear above 100°C, when bubbles form, and degrade the quality and accuracy of MRI-based thermometry, making reliable temperature mapping impossible [69]. For this reason, we prioritized accurate thermal measurements by MRI over replicating full clinical power settings.

5. Conclusion

This study presents analytical and hybrid models for simulating temperature distributions during thermoablative procedures (MWA, LITT, and RFA). The proposed model is clearly an approximation and is not intended to provide a fully accurate representation of the complex thermal dynamics occurring during ablation. Its primary strength lies in its computational efficiency and in the potential to provide fast, voxel-level estimations of temperature fields based on limited MRI data while also offering a framework that can be aligned with MRI thermometry to directly connect simulations with experimental measurements in a practical workflow. Although its current version is not yet ready for clinical application in real time, it offers a promising foundation for further development. Future improvements will focus on optimizing time synchronization and incorporating perfusion models for *in vivo* applications, enhancing the model precision, particularly in complex tissues. The model provides a valuable framework for exploring optimization strategies and guiding future developments toward computationally efficient and clinically relevant thermal monitoring tools.

Disclosure statement

No potential conflict of interest was reported by the author(s).

Funding

This study was financed in part by the Coordenação de Aperfeiçoamento de Pessoal de Nível Superior – Brasil (CAPES) – Finance Code 001. Financial support was also provided by the RRI BEST, Industrie du Futur, and the RRI IMPACT, both at the University of Bordeaux. This work received financial support from the French National Investments: ANR-24-CE92-0073 (SMART-HEAT project). Additionally, this project has received financial support from the CNRS through the MITI interdisciplinary programs under its exploratory research program (projet CHAUPATAT). This research was also supported by the Conselho Nacional de Desenvolvimento Científico e Tecnológico (CNPq) – Brasil, under grant number 400890/2019-4, through Call No. 01/2019 for the Support of Doctoral Training in Strategic Areas.

ORCID

Mariana De Melo Antunes http://orcid.org/0000-0001-9704-746X
Ida Burgers http://orcid.org/0009-0001-2160-6875
Valéry Ozenne http://orcid.org/0000-0002-7883-756X
Luigi Nardone http://orcid.org/0009-0004-2783-3288
Max Seidensticker http://orcid.org/0000-0002-2481-5410
Olaf Dietrich http://orcid.org/0000-0001-6182-5039
Manon Desclides http://orcid.org/0000-0002-5735-8420
Bruno Quesson http://orcid.org/0000-0001-6434-3684
Andrzej Kusiak http://orcid.org/0000-0002-1931-7230
Sandro Metrevelle Marcondes de Lima e Silva http://orcid.org/0000-0002-1295-6208
Jean-Luc Battaglia http://orcid.org/0000-0003-1176-5714

Data availability statement

The data that support the findings of this study are available from the corresponding author upon reasonable request.

References

[1] Grieco CA, Simon CJ, Mayo-Smith WW, et al. Image-guided percutaneous thermal ablation for the palliative treatment of chest wall masses. Am J Clin Oncol. 2007;30(4):361–367. doi: 10.1097/COC.0b013e318033e76a.
[2] Cutsem EV, Cervantes A, Adam R, et al. ESMO consensus guidelines for the management of patients with metastatic colorectal cancer. Ann Oncol. 2016;27(8):1386–1422. doi: 10.1093/annonc/mdw235.
[3] Vogel A, Cervantes A, Chau I, et al. Hepatocellular carcinoma: ESMO clinical practice guidelines for diagnosis, treatment and follow-up. Ann Oncol. 2018;29(Suppl 4):iv238–iv255. doi: 10.1093/annonc/mdy308.
[4] Gennari A, André F, Barrios CH, et al. ESMO clinical practice guideline for the diagnosis, staging and treatment of patients with metastatic breast cancer. Ann Oncol. 2021;32(12):1475–1495. doi: 10.1016/j.annonc.2021.09.019.
[5] McDannold N, Tempany CM, Fennessy FM, et al. Uterine leiomyomas: MR imaging–based thermometry and thermal dosimetry during focused ultrasound thermal ablation. Radiology. 2006;240(1):263–272. doi: 10.1148/radiol.2401050717.
[6] Denis de Senneville B, Mougenot C, Quesson B, et al. MR thermometry for monitoring tumor ablation. Eur Radiol. 2007;17(9):2401–2410.
[7] Ozenne V, Toupin S, Bour P, et al. Improved cardiac magnetic resonance thermometry and dosimetry for monitoring lesion formation during catheter ablation. Magn Reson Med. 2017;77(2):673–683. doi: 10.1002/mrm.26158.
[8] Munier SM, Hargreaves EL, Patel NV, et al. Effects of variable power on tissue ablation dynamics during magnetic resonance-guided laser-induced thermal therapy with the visualase system. Int J Hyperthermia. 2018;34(6):764–772. doi: 10.1080/02656736.2017.1376355.
[9] Geoghegan R, Ter Haar G, Nightingale K, et al. Methods of monitoring thermal ablation of soft tissue tumors–a comprehensive review. Med Phys. 2022;49(2):769–791. doi: 10.1002/mp.15439.
[10] Öcal O, Dietrich O, Lentini S, et al. Predicting liver ablation volumes with real-time MRI thermometry. JHEP Rep. 2024;6(11):101199. doi: 10.1016/j.jhepr.2024.101199.
[11] Do TD, Haas A, Vollherbst DF, et al. Semi-automatic artifact quantification in thermal ablation probe and algorithms for the evaluation of metal artifact reduction. Int J Hyperther. 2023;40(1):2205071. doi: 10.1080/02656736.2023.2205071.
[12] Munier SM, Desai AN, Patel NV, et al. Effects of intraoperative magnetic resonance thermal imaging signal artifact during laser interstitial thermal therapy on thermal damage estimate and postoperative magnetic resonance imaging ablative area concordance. Operative Surg. 2020;18(5):524–530. doi: 10.1093/ons/opz182.
[13] Munier SM, Liang AS, Desai AN, et al. Characterization of magnetic resonance thermal imaging signal artifact during magnetic resonance guided laser-induced thermal therapy. Operative Surg. 2020;19(5):619–624. doi: 10.1093/ons/opaa229.
[14] Vincelette RL, Curran MP, Danish SF, et al. Appearance and modeling of bubble artifacts in intracranial magnetic resonance-guided laser interstitial thermal therapy (MRG-LITT) temperature images. Magn Reson Imaging. 2023;101:67–75. doi: 10.1016/j.mri.2023.03.022.
[15] Tian Z, Cheng Y, Hu H, et al. Numerical study on the effect of bifurcation vessel parameters on microwave ablation of lung tissue. Electromagn Biol Med. 2022;41(3):272–280. doi: 10.1080/15368378.2022.2065680.
[16] Trujillo M, Berjano E. Review of the mathematical functions used to model the temperature dependence of electrical and thermal conductivities of biological tissue in radiofrequency ablation. Int J Hyperthermia. 2013;29(6):590–597. doi: 10.3109/02656736.2013.807438.

[17] Gonzalez-Suarez A, Berjano E. Comparative analysis of different methods of modeling the thermal effect of circulating blood flow during rf cardiac ablation. IEEE Trans Biomed Eng. 2016;63(2):250–259. doi: 10.1109/TBME.2015.2451178.
[18] Harvan HJ, Wahyudi S, Winarto. Microwave ablation therapy for hepatocellular carcinoma: the effect of metabolic heat on temperature distribution. ARFMTS. 2024;118(2):24–33. doi: 10.37934/arfmts.118.2.2433.
[19] Ai H, Wu S, Gao H, et al. Temperature distribution analysis of tissue water vaporization during microwave ablation: experiments and simulations. Int J Hyperthermia. 2012;28(7):674–685. doi: 10.3109/02656736.2012.710769.
[20] Zhang X, Wei W, Qian L, et al. Real-time monitoring of bioelectrical impedance for minimizing tissue carbonization in microwave ablation of porcine liver. Sci Rep. 2024;14(1):30404. doi: 10.1038/s41598-024-80725-3.
[21] Fuentes D, Cardan R, Stafford RJ, et al. High-fidelity computer models for prospective treatment planning of radiofrequency ablation with in vitro experimental correlation. J Vasc Interv Radiol. 2010;21(11):1725–1732. doi: 10.1016/j.jvir.2010.07.022.
[22] Feras Marqa M, Mordon S, Betrouni N. Laser interstitial thermotherapy of small breast fibroadenomas: numerical simulations. Lasers Surg Med. 2012;44(10):832–839.
[23] Mitchell D, Fahrenholtz S, MacLellan C, et al. A heterogeneous tissue model for treatment planning for magnetic resonance-guided laser interstitial thermal therapy. Int J Hyperther. 2018;34(7):943–952. doi: 10.1080/02656736.2018.1429679.
[24] López-Aguirre M, Caballero-Insaurriaga J, Urso D, et al. Lesion 3D modeling in transcranial MR-guided focused ultrasound thalamotomy. Magn Reson Imaging. 2021;80:71–80. doi: 10.1016/j.mri.2021.04.003.
[25] Audigier C, Mansi T, Delingette H, et al. Efficient lattice boltzmann solver for patient-specific radiofrequency ablation of hepatic tumors. IEEE Trans Med Imaging. 2015;34(7):1576–1589. doi: 10.1109/TMI.2015.2406575.
[26] Voglreiter P, Mariappan P, Pollari M, et al. RFA guardian: comprehensive simulation of radiofrequency ablation treatment of liver tumors. Sci Rep. 2018;8(1):787. doi: 10.1038/s41598-017-18899-2.
[27] Chiang J, Wang P, Brace CL. Computational modelling of microwave tumour ablations. Int J Hyperthermia. 2013;29(4):308–317. doi: 10.3109/02656736.2013.799295.
[28] Deshazer G, Hagmann M, Merck D, et al. Computational modeling of 915 MHz microwave ablation: comparative assessment of temperature-dependent tissue dielectric models. Med Phys. 2017;44(9):4859–4868. doi: 10.1002/mp.12359.
[29] Chen R, Lu F, Wu F, et al. An analytical solution for temperature distributions in hepatic radiofrequency ablation incorporating the heatsink effect of large vessels. Phys Med Biol. 2018;63(23):235026. doi: 10.1088/1361-6560/aaeef9.
[30] López Molina JA, Rivera MJ, Berjano E. Electricalthermal analytical modeling of monopolar rf thermal ablation of biological tissues: determining the circumstances under which tissue temperature reaches a steady state. Math Biosci Eng. 2016;13(2):281–301. doi: 10.3934/mbe.2015003.
[31] Roca Oria EJ, Bergues Cabrales LE, Bory Reyes A J. Analytical solution of the bioheat equation for thermal response induced by any electrode array in anisotropic tissues with arbitrary shapes containing multipletumor nodules. Rev Mex Fís. 2019;65(3 May–Jun):284–290. doi: 10.31349/RevMexFis.65.284.
[32] Wang K, Tavakkoli F, Wang S, et al. Analysis and analytical characterization of bioheat transfer during radiofrequency ablation. J Biomech. 2015;48(6):930–940. doi: 10.1016/j.jbiomech.2015.02.023.
[33] Ahmadi M, Biswas D, Lin M, et al. Physics-informed machine learning for advancing computational medical imaging: integrating datadriven approaches with fundamental physical principles. Artif Intell Rev. 2025;58:297.
[34] Sadatamin S, Ketabi S, DonszelmannLund E, et al. Enhancing MR guided laser interstitial thermal therapy planning using UNET: a datadriven approach for predicting MR thermometry images. Proc of SPIE. 2024;12928:344–349
[35] Schulmann N, SoltaniSarvestani MA, De Landro M, et al. Modelbased thermometry for laser ablation procedure using Kalman filters and sparse temperature measurements. IEEE Trans Biomed Eng. 2022;69(9):2839–2849. doi: 10.1109/TBME.2022.3155574.
[36] Fuentes D, Feng Y, Elliott A, et al. Adaptive real-time bioheat transfer models for computer-driven MR-guided laser induced thermal therapy. IEEE Trans Biomed Eng. 2010;57(5):1024–1030. doi: 10.1109/TBME.2009.2037733.
[37] Frackowiak B, Van den Bosch V, Tokoutsi Z, et al. First validation of a model-based hepatic percutaneous microwave ablation planning on a clinical dataset. Sci Rep. 2023;13(1):18918. doi: 10.1038/s41598-023-45924-4.
[38] Reddy Upendra R, Simon R, Linte CA. A deep learning framework for image super-resolution for late gadolinium enhanced cardiac MRI. Comp Cardiol. 2021;48:1–4.
[39] Pennes HH. Analysis of tissue and arterial blood temperatures in the resting human forearm. J Appl Physiol. 1948;1(2):93–122. doi: 10.1152/jappl.1948.1.2.93.
[40] Stehfest. Algorithm 368, numerical inversion of Laplace transforms [d5]. Technical report, Institut f. Angew. Physik, J. W. Goethe Unviersität; 1970.
[41] Carslaw HS, Jaeger JC. Conduction of heat in solids. 2nd ed. Oxford: Oxford University Press; 1959.
[42] Necati Ozisik M. Heat conduction. 2nd ed. New York: John Wiley & Sons; 1993.
[43] Odeen H, Parker DL. Magnetic resonance thermometry and its biological applications-physical principles and practical considerations. Prog Nucl Magn Reson Spectrosc. 2019;110:34–61. doi: 10.1016/j.pnmrs.2019.01.003.
[44] Peters RD, Scott Hinks R, Mark Henkelman R. Heat-source orientation and geometry dependence in proton-resonance frequency shift magnetic resonance thermometry. Magn Reson Med. 1999;41(5):909–918.

[45] Hoffmann R, Rempp H, Eibofner F, et al. In vitro artefact assessment of a new MR-compatible microwave antenna and a standard MR-compatible radiofrequency ablation electrode for tumour ablation. Eur Radiol. 2016;26(3):771–779.
[46] Lewin JS, Duerk JL, Jain VR, et al. Needle localization in MR-guided biopsy and aspiration: effects of field strength, sequence design, and magnetic field orientation. AJR Am J Roentgenol. 1996;166(6):1337–1345. doi: 10.2214/ajr.166.6.8633445.
[47] Yon M, Delcey M, Bour P, et al. Continuous cardiac thermometry via simultaneous catheter tracking and undersampled radial golden angle acquisition for radiofrequency ablation monitoring. Sci Rep. 2022;12(1):4006. doi: 10.1038/s41598-022-06927-9.
[48] Jezzard P, Clare S. Sources of distortion in functional MRI data. Hum Brain Mapp. 1999;8(2–3):80–85. doi: 10.1002/(SICI)1097-0193(1999)8:2/3<80::AID-HBM2>3.0.CO;2-C.
[49] Butts K, Pauly JM, Daniel BL, et al. Management of biopsy needle artifacts: techniques for RF-refocused MRI. J Magn Reson Imaging. 1999;9(4):586–595. doi: 10.1002/(SICI)1522-2586(199904)9:4<586::AID-JMRI13>3.0.CO;2-X.
[50] Silva NP, Bottiglieri A, Conceição RC, et al. Characterisation of ex vivo liver thermal properties for electromagnetic-based hyperthermic therapies. Sensors. 2020;20(10):3004. doi: 10.3390/s20103004.
[51] Zhang M, Che Z, Chen J, et al. Experimental determination of thermal conductivity of water − agar gel at different concentrations and temperatures. J Chem Eng Data. 2011;56(4):859–864. doi: 10.1021/je100570h.
[52] Lemmon EW, McLinden MO, Friend DG. Thermophysical properties of fluid systems in NIST chemistry webbook. 2005. Available from: http://webbook.nist.gov.
[53] Avants NTBB, Johnson H. Advanced normalization tools (ants). Technical report, University of Pennsylvania, University of Virginia and University of Iowa; 2014.
[54] Roger F. Restricted step methods. In: Practical methods of optimization. 2nd ed. New York: Wiley; 1987. Originally published in 1980.
[55] Desclides M, Ozenne V, Bour P, et al. Real-time automatic temperature regulation during in vivo MRI-guided laser induced thermotherapy (MR-LITT). Sci Rep. 2023;13(1):3279. doi: 10.1038/s41598-023-29818-z.
[56] Wang Y, Jin J, Boppart SA. Model-based real-time estimation of tissue thermal properties and temperature distribution using Kalman filtering. IEEE Trans Biomed Eng. 2022;69(10):2913–2923.
[57] Zhang J, Hills J, Zhong Y, et al. Modeling of soft tissue thermal damage based on GPU acceleration. Comp Assist Surg. 2019;24(sup1):5–12. doi: 10.1080/24699322.2018.1557891.
[58] Borsic A, Hoffer E, Attardo EA. GPU-accelerated real time simulation of radio frequency ablation thermal dose. Paper presented at: Proceedings of SPIE Medical Imaging. SPIE; 2012. p. 1–10.
[59] Rieder C, Kröger T, Schumann C, et al. GPU-based real-time approximation of the ablation zone for radiofrequency ablation. IEEE Trans Vis Comput Graphics. 2011;17(12):1811–1822.
[60] Chen G, Stang J, Haynes M, et al. Real-time 3D microwave monitoring of interstitial thermal therapy. IEEE Trans Biomed Eng. 2017;64(12):2880–2889.
[61] Mariappan P, Weir P, Flanagan R, et al. GPU-based RFA simulation for minimally invasive cancer treatment of liver tumours. Int J Comput Assist Radiol Surg. 2016;11:1231–1242.
[62] Hoffer EK, Borsic A, Patel SD. Validation of software for patient-specific real-time simulation of hepatic radiofrequency ablation. J Assoc Univ Radiol. 2021;18(2):101–110.
[63] Bhattacharya A, Mahajan RL. Temperature dependence of thermal conductivity of biological tissues. Physiol Meas. 2003;24(3):769–783. doi: 10.1088/0967-3334/24/3/312.
[64] Bianchi L, Cavarzan F, Ciampitti L, et al. Thermophysical and mechanical properties of biological tissues as a function of temperature: a systematic literature review. Int J Hyperthermia. 2022;39(1):297–340. doi: 10.1080/02656736.2022.2028908.
[65] Mohammadi A, Bianchi L, Korganbayev S, et al. Thermomechanical modeling of laser ablation therapy of tumors: sensitivity analysis and optimization of influential variables. IEEE Trans Biomed Eng. January. 2022;69(1):302–313. doi: 10.1109/TBME.2021.3092889.
[66] Sebek J, Albin N, Bortel R, et al. Sensitivity of microwave ablation models to tissue biophysical properties: a first step toward probabilistic modeling and treatment planning. Med Phys. 2016;43(5):2649–2661. doi: 10.1118/1.4947482.
[67] Hall SK, Ooi EH, Payne SJ. Cell death, perfusion and electrical parameters are critical in models of hepatic radiofrequency ablation. Int J Hyperther. 2015;31(5):538–550. doi: 10.3109/02656736.2015.1032370.
[68] Ye Q, Wang J, Deng Z-C, et al. Measurement of the complex refractive index of tissue-mimicking phantoms and biotissue by extended differential total reflection method. J Biomed Opt. 2011;16(9):097001. doi: 10.1117/1.3615657.
[69] Viallon M, Terraz S, Roland J, et al. Observation and correction of transient cavitation-induced PRFS thermometry artifacts during radiofrequency ablation, using simultaneous ultrasound/MR imaging. Med Phys. 2010;37(4):1491–1506. doi: 10.1118/1.3309439.
[70] Knight De Hoog JH, Stokes AN. An improved method for numerical inversion of Laplace transforms. Philadelphia (PA): Society for Industrial and Applied Mathematics; 1982.
[71] Gaver DPJr. Observing stochastic processes, and approximate transform inversion. Informs. 1966;14(3):361–553.
[72] Peter Den Iseger. Numerical transform inversion using gaussian quadrature. Cambridge: Cambridge University Press; 2006.

Appendix A: Resolution of the heat diffusion model

Equations (1)–(4) are solved using a hybrid technique involving the Laplace Transform and finite differences according to the expression of the source from relations (5), (6) or (7).

Step 1: Change of variable

To solve the equation, a first change of variables is made as: $T'(r,t)=T(r,t)-T_b$. This leads to modifying the Equations (1) to (4) as:

$$\rho C_p \frac{\partial T'(r,t)}{\partial t} = k\left(\frac{\partial^2 T'(r,t)}{\partial r^2}+\frac{2}{r}\frac{\partial T'(r,t)}{\partial r}\right)-\rho_b C_b \omega_b T' + Q(r,t) \tag{A.1}$$

$$BC_1: T'(r,t) \to \text{finite, at } r=0, t>0 \tag{A.2}$$

$$BC_2: T'(r,t)=0, \text{at } r\to\infty, t>0 \tag{A.3}$$

$$IC: T'(r,t)=0, \text{for } 0\le r<\infty, t=0 \tag{A.4}$$

A second change of variables is applied as: $U(t)=rT'(r,t)$. Therefore, we have:

$$T'(r,t)=\frac{U(r,t)}{r},\quad \frac{\partial T'(r,t)}{\partial t}=\frac{1}{r}\frac{\partial U(r,t)}{\partial t},\quad \frac{\partial T'(r,t)}{\partial r}=-\frac{1}{r^2}U(r,t)+\frac{1}{r}\frac{\partial U(r,t)}{\partial r},$$

$$\frac{\partial^2 T'(r,t)}{\partial r^2}=-\frac{1}{r^2}\frac{\partial U(r,t)}{\partial r}+\frac{1}{r}\frac{\partial^2 U(r,t)}{\partial r^2}-\frac{1}{r^2}\frac{\partial U(r,t)}{\partial r}+\frac{2}{r^3}U(r,t)$$

Replacing these expressions in relations (A.1) to (A.4) leads to:

$$\rho C_p \frac{1}{r}\frac{\partial U(r,t)}{\partial t} = k\left(-\cancel{\frac{2}{r^2}\frac{\partial U(r,t)}{\partial r}}+\frac{1}{r}\frac{\partial^2 U(r,t)}{\partial r^2}+\cancel{\frac{2}{r^3}U(r,t)}+\cancel{\frac{2}{r^3}U(r,t)}+\cancel{\frac{2}{r^2}\frac{\partial U(r,t)}{\partial r}}\right) - \rho_b C_b \omega_b \frac{U(r,t)}{r} + Q(r,t) \tag{A.5}$$

$$BC_1: U(r,t)=0, \text{at } r=0, t>0 \tag{A.6}$$

$$BC_2: U(r,t)=0, \text{at } r\to\infty, t>0 \tag{A.7}$$

$$IC: U(r,t)=0, \text{for } 0\le r<\infty, t=0 \tag{A.8}$$

Finally, Equation (A.5) can be simplified as:

$$\frac{1}{\alpha}\frac{\partial U(r,t)}{\partial t}=\frac{\partial^2 U(r,t)}{\partial r^2}-\frac{\rho_b C_b \omega_b}{k}U(r,t)+\frac{r}{k}Q(r,t) \tag{A.9}$$

The resulting equation is similar to the one-directional heat transfer equation in a rectangular coordinate system.

Step 2: Application of the Laplace transform

Then the Laplace transform, defined as follows, can be applied:

$$\theta(r,p)=\mathcal{L}_t\left[U(r,t)\right]=\int_0^\infty U(r,t)e^{-pt}\,dt \tag{A.10}$$

Applying this integral transform on relations (A.6) to (A.9), using the IC (A.8), and considering that $Q(r,p)=Q_0(r)\delta(t)$, leads to:

$$\frac{p}{\alpha}\theta(r,p)=\frac{\partial^2\theta(r,p)}{\partial r^2}-\frac{\rho_b C_b \omega_b}{k}\theta(r,p)+\frac{r}{k}Q_0(r) \tag{A.11}$$

$$BC_1: \theta(r,p) = 0, \text{at } r = 0 \tag{A.12}$$

$$BC_2: \theta(r,p) = 0, \text{when } r \to \infty \tag{A.13}$$

Equation (A.11) is then rewritten as:

$$\frac{\partial^2 \theta(r,p)}{\partial r^2} - K^2 \theta(r,p) = -\frac{r}{k} Q_0(r) \tag{A.14}$$

with:

$$K^2 = \frac{\rho_b C_b \omega_b}{k} + \frac{p}{\alpha} \tag{A.15}$$

In this case, the solution of the homogeneous equation is:

$$\theta_h(r,p) = C_1 e^{-Kr} + C_2 e^{Kr} \tag{A.16}$$

The complementary solution will depend on the expression of $Q_0(r)$. Three approaches for modeling the electromagnetic heat source are proposed, and their solutions are presented in the following sections.

Beer-Lambert absorption law (LITT)

The radial heat source distribution is described following the Beer-Lambert law as:

$$Q_0(r) = Q_1 e^{-\beta_1 r} \tag{A.17}$$

Therefore the complementary solution can be obtained using:

$$\theta_c(r,p) = (A + Br) e^{-\beta_1 r} \tag{A.18}$$

Thus:

$$\frac{\partial \theta_c}{\partial r} = B e^{-\beta_1 r} - (A + Br) \beta_1 e^{-\beta_1 r} \tag{A.19}$$

and:

$$\frac{\partial \theta_c^2}{\partial r^2} = -\beta_1 B e^{-\beta_1 r} - B \beta_1 e^{-\beta_1 r} + (A + Br) \beta_1^2 e^{-\beta_1 r} \tag{A.20}$$

$$= -2\beta_1 B e^{-\beta_1 r} + (A + Br) \beta_1^2 e^{-\beta_1 r} \tag{A.21}$$

In Equation (A.14):

$$-2\beta_1 B e^{-\beta_1 r} + (A + Br) \beta_1^2 e^{-\beta_1 r} - K^2 (A + Br) e^{-\beta_1 r} = -\frac{r}{k} Q_1 e^{-\beta_1 r} \tag{A.22}$$

Therefore:

$$-2\beta_1 B + (A + Br) \beta_1^2 - K^2 (A + Br) = -\frac{r}{k} Q_1 \tag{A.23}$$

Which means:

$$-2\beta_1 B + A\beta_1^2 - AK^2 = 0 \tag{A.24}$$

And:

$$B\beta_1^2 - K^2 B = -\frac{Q_1}{k} \tag{A.25}$$

Finally:

$$B = -\frac{Q_1}{k(\beta_1^2 - K^2)} \tag{A.26}$$

And:

$$A = \frac{-2\beta_1 Q_1}{k\left(\beta_1^2 - K^2\right)^2} \tag{A.27}$$

So, the general solution is:

$$\theta(r,p) = C_1 e^{-Kr} + C_2 e^{Kr} - \frac{Q_1}{k\left(\beta_1^2 - K^2\right)}\left(\frac{2\beta_1}{\left(\beta_1^2 - K^2\right)} + r\right)e^{-\beta_1 r} \tag{A.28}$$

Using $BC_2(r \to \infty)$:

$$C_2 = 0 \tag{A.29}$$

And using $BC_1(r = 0)$:

$$C_1 = \frac{2\beta_1 Q_1}{k\left(\beta_1^2 - K^2\right)^2} \tag{A.30}$$

We find the general solution as:

$$\boxed{\theta(r,p) = \frac{Q_1}{k}\frac{2\beta_1 e^{-Kr} + \left(\left(K^2 - \beta_1^2\right)r - 2\beta_1\right)e^{-\beta_1 r}}{\left(K^2 - \beta_1^2\right)^2}} \tag{A.31}$$

Uniform absorption (RFA)

We consider a uniform heat source distribution, defined as:

$$Q_{EM}(r) = Q_0 \Pi_{r_0}(r) \tag{A.32}$$

Where $\Pi_{r_0}(r) = H(r) - H(r - r_0)$ and $H(r)$ denotes the Heaviside function. This relation implies that the heat source is constant in domain bounded by $0 \le r \le r_0$.

Inside the Interval ($0 \le r \le r_0$)

In this interval, the heat source is constant, i.e. $Q_0 \Pi_{r_0}(r) = Q_0$. Thus, the equation for $\theta(r,p)$ in the interval $0 \le r \le r_0$ becomes:

$$\frac{\partial^2 \theta_c(r,p)}{\partial r^2} - K^2 \theta_c(r,p) = -\frac{rQ_0}{k} \tag{A.33}$$

The particular solution can be tried in the form:

$$\theta_c(r,p) = A + Br \tag{A.34}$$

Substituting this form into the equation, we have:

$$-K^2(A + Br) = -\frac{rQ_0}{k} \tag{A.35}$$

This implies that:

$$B = \frac{Q_0}{kK^2} \tag{A.36}$$

and

$$A = 0 \tag{A.37}$$

Therefore, the particular solution inside the interval $0 \le r \le r_0$ is:

$$\theta_c(r,p) = \frac{Q_0 r}{kK^2} \tag{A.38}$$

Using the condition $\theta(0,p) = 0$, we find that $C_1 = 0$, so the homogeneous solution inside the interval becomes:

$$\theta_h(r,p) = C_2 e^{Kr} \tag{A.39}$$

For $0 \le r \le r_0$, we have:

$$\theta(r,p) = C_2 e^{Kr} + \frac{Q_0 r}{kK^2} \tag{A.40}$$

Outside the Interval ($r > r_0$)

Outside the interval (when $r > r_0$), the heat source is zero, so the equation becomes:

$$\frac{\partial^2 \theta_c(r,p)}{\partial r^2} - K^2 \theta_c(r,p) = 0 \tag{A.41}$$

The solution to this equation is:

$$\theta_c(r,p) = C_3 e^{-Kr} + C_4 e^{Kr} \tag{A.42}$$

Since the term $C_4 e^{Kr}$ would diverge as $r \to \infty$, we impose $C_4 = 0$, so the solution outside the interval is:

$$\theta_c(r,p) = C_3 e^{-Kr} \tag{A.43}$$

For $r > r_0$, we have:

$$\theta(r,p) = C_3 e^{-Kr} \tag{A.44}$$

Solution for the entire domain

The continuity of $\theta(r,p)$ at $r = r_0$ requires that $\theta_{r \le r_0}(r_0,p) = \theta_{r > r_0}(r_0,p)$. That is:

$$C_2 e^{Kr_0} + \frac{Q_0 r_0}{kK^2} = C_3 e^{-Kr_0} \tag{A.45}$$

The derivative of $\theta(r,p)$ for $0 \le r \le r_0$ is:

$$\frac{\partial \theta(r,p)}{\partial r} = C_2 K e^{Kr} + \frac{Q_0}{kK^2} \tag{A.46}$$

For $r > r_0$, the derivative is:

$$\frac{\partial \theta(r,p)}{\partial r} = -C_3 K e^{-Kr} \tag{A.47}$$

The continuity of the derivative of $\theta(r,p)$ at $r = r_0$ requires that:

$$\left.\frac{\partial \theta(r,p)}{\partial r}\right|_{(\text{for } r \le r_0)} = \left.\frac{\partial \theta(r,p)}{\partial r}\right|_{(\text{for } r > r_0)} \tag{A.48}$$

That is:

$$C_2 K e^{Kr_0} + \frac{Q_0}{kK^2} = -C_3 K e^{-Kr_0} \tag{A.49}$$

Now we have the system of equations for the constants C_2 and C_3:

$$\begin{cases} C_2 e^{Kr_0} + \dfrac{Q_0 r_0}{kK^2} = C_3 e^{-Kr_0} \\ C_2 K e^{Kr_0} + \dfrac{Q_0}{kK^2} = -C_3 K e^{-Kr_0} \end{cases} \tag{A.50}$$

We multiply the first equation by K and sum the two equations in order to eliminate C_3:

$$2C_2 K e^{Kr_0} + \frac{Q_0}{kK^2}(1 + Kr_0) = 0 \tag{A.51}$$

$$C_2 = \left(\frac{-Q_0}{kK^2}(1+Kr_0)\right)\left(\frac{1}{2Ke^{Kr_0}}\right) = \frac{-Q_0}{2kK^3e^{Kr_0}}(1+Kr_0) \tag{A.52}$$

and

$$C_3 = \left(\frac{-Q_0}{2kK^2}(1-Kr_0)\right)\left(\frac{1}{Ke^{-Kr_0}}\right) = \frac{-Q_0e^{Kr_0}}{2kK^3}(1-Kr_0) \tag{A.53}$$

The general solution for $\theta(r,p)$ is:

$$\boxed{\theta(r,p) = \begin{cases} -\dfrac{Q_0}{2kK^3e^{Kr_0}}(1+Kr_0)e^{Kr} + \dfrac{Q_0 r}{kK^2} \text{ for } 0 \le r \le r_0 \\ -\dfrac{Q_0e^{Kr_0}}{2kK^3}(1-Kr_0)e^{-Kr} \text{ for } r > r_0 \end{cases}} \tag{A.54}$$

Modified absorption law (MWA)

We consider a modified absorption law suitable with the MWA process as:

$$Q_0(r) = Q_2\, e^{-\beta_2\sqrt{r}} \tag{A.55}$$

The solution is achieved by applying a finite difference scheme based on the relation (A.14) with N nodes as:

$$\frac{\theta_{i+1} - 2\theta_i + \theta_{i-1}}{\Delta r^2} - K^2\theta_i = -\frac{r}{k}Q_2\, e^{-\beta\sqrt{r}}, i = 2, N-1 \tag{A.56}$$

It can be expressed as:

$$\theta_{i+1} + G\theta_i + \theta_{i-1} = -\frac{r}{k}\Delta r^2 Q_2\, e^{-\beta\sqrt{r}}, \; i = 2, N-1 \tag{A.57}$$

with:

$$G = -2 - K^2\Delta r^2, K^2 = \frac{\rho_b C_b \omega_b}{k} + \frac{p}{\alpha} \tag{A.58}$$

and the conditions:

$$\theta_1 = 0; \theta_N = 0; \tag{A.59}$$

Thus, the temperature distribution comes to solve the following linear system:

$$\begin{bmatrix} 10^7 & & & & & & & \\ 1 & G & 1 & & & & & \\ & 1 & G & 1 & & & & \\ & & 1 & G & 1 & & & \\ & & & \ddots & \ddots & \ddots & & \\ & & & & 1 & G & 1 & \\ & & & & & & 10^7 & \end{bmatrix} \begin{bmatrix} \theta_1 \\ \vdots \\ \vdots \\ \vdots \\ \vdots \\ \vdots \\ \theta_N \end{bmatrix} = -\frac{r}{k}\Delta r^2 Q_2\, e^{-\beta\sqrt{r}} \begin{bmatrix} 0 \\ 1 \\ 1 \\ 1 \\ \vdots \\ 1 \\ 0 \end{bmatrix} \tag{A.60}$$

For the two prescribed temperatures at the two boundaries of the domain, a penalization technique is applied as shown in the previous relation.

Inverse Laplace transform

The function $U(r,t)$ is obtained by applying the inverse Laplace transform on $\theta(r,p)$. Several efficient and fast techniques can be used [40,70–72]. The Stehfest method provides an efficient way to approximate the inverse Laplace transform through a weighted summation as:

$$U(r,t) \approx \frac{\ln(2)}{t} \sum_{i=1}^{N} V_i \theta\left(r, \frac{i \ln(2)}{t}\right) \tag{A.61}$$

where N is an even integer, and V_i are weighting coefficients determined by:

$$V_i = \sum_{k=\max(1,i/2)}^{\min(i,N/2)} \frac{k^{N/2}}{(N/2)!} \frac{(2k)!}{(N/2-k)!(k-1)!(i-k)!(2k-i)!} \tag{A.62}$$

This method, derived from the Post-Widder formula, allows for a practical, accurate inversion without the need for extensive sampling intervals, making it a robust choice for integrating heat sources in transient thermal analyses.

The impulse response is therefore calculated from the relation:

$$h(r,t) = \frac{U(r,t)}{r} \tag{A.63}$$

For a time-varying heat source such as $Q(r,t) = Q_0(r)\psi(t)$, the temperature $T(r,t)$ is calculated using the convolution product between the impulse response and the heat source as:

$$T(r,t) = \int_0^{\infty} h(r,t-\tau)\,\psi(\tau)\,\mathrm{d}\tau \tag{A.64}$$

Alternatively, this convolution can also be obtained faster as:

$$T(r,t) = \mathcal{L}^{-1}\left\{\theta(r,p) \times Q(p)\right\} \tag{A.65}$$

However, this last formulation suggests that the Laplace transform of $\psi(t)$ can be easily calculated, which is only true for specific transient waveforms. Therefore, the relation (A.64) should be considered instead, and the convolution is calculated efficiently using an FFT.